The response regulator BqsR/CarR controls ferrous iron (Fe^{2+}) acquisition in *Pseudomonas aeruginosa*

Alexander Paredes[1†], Mackenzie Hull[2†], Harvinder Singh[1], Darryn Greene[1], Alexis J. Northrup[2], Aya Kubo[2], Janae Baptiste Brown[3], Kelly N. Chacón[4], Marianna A. Patrauchan[2], and Aaron T. Smith[1*]

[1]Department of Chemistry and Biochemistry, University of Maryland, Baltimore County, Baltimore, Maryland, 21250 USA

[2]Department of Microbiology and Molecular Genetics, Oklahoma State University, Stillwater, Oklahoma, 74078 USA

[3]Department of Chemistry and Biochemistry, Spelman College, Atlanta, Georgia, 30314 USA

[4]Department of Chemistry, Reed College, Portland, Oregon, 97202 USA

[†]These authors contributed equally to this work.

[*]To whom correspondence should be addressed. Tel: 410-455-1985; E-mail: smitha@umbc.edu

Abstract

Pseudomonas aeruginosa is a ubiquitous, Gram-negative bacterium that forms biofilms and is responsible for antibiotic-resistant nosocomial infections in humans. The *P. aeruginosa* BqsRS two-component system regulates biofilm formation and dispersal by sensing extracytoplasmic Fe^{2+}, but the mechanistic details of this process are poorly understood. In this work, we report the crystal and solution structures of the *Pa*BqsR response regulator receiver domain, comprising a $(\beta\alpha)_5$ response regulator assembly, and the DNA-binding domain, comprising a helix-turn-helix motif. Consistent with its cognate stimulus being Fe^{2+}, we show that *Pa*BqsR binds directly to the promoter region of the *feo* operon that encodes the bacterial Fe^{2+} transport system FeoABC. Corroborating these *in vitro* results, transcriptional studies show that *Pa*BqsR is a global regulator controlling many important genes in PAO1, including the *feo* operon. Intriguingly, promoter-based assays reveal that *Pa*BqsR is a dynamic regulator that responds to bioavailable Fe^{2+}, likely through the ability of *Pa*BqsR to bind Fe^{2+} directly via a His-rich motif, independent of the *Pa*BqsS membrane His kinase. This mode of regulation is unprecedented among OmpR-like response regulators but represents an important level of control over Fe^{2+} acquisition in *P. aeruginosa* that could be an attractive therapeutic target to treat nosocomial infections.

Keywords

biofilms; two-component system; signal transduction; iron; Feo

Abbreviations

ANR, anaerobic transcriptional regulator; CF, cystic fibrosis; CV, column volumes; DBD, DNA-binding domain of *Pa*BqsR; EMSA, electrophoretic mobility shift assays; EXAFS, extended X-ray absorption fine structure; FI, fit index; FUR, ferric uptake regulator; IMAC, immobilized metal affinity chromatography; ICP-MS, inductively couple plasmon mass spectrometry; IPTG, isopropyl β-D-1-thiogalactopyranoside; LB, Luria broth; HK, membrane sensor histidine kinase; MWCO, molecular weight cutoff; RD, N-terminal receiver domain; NMR, nuclear magnetic resonance; NOESY, nuclear Overhauser effect spectroscopy; OD, optical density; PMSF, phenylmethylsulfonyl fluoride; RNA-seq, RNA sequencing; RR, response regulator; SEC, size-exclusion chromatography; TEV, tobacco etch virus; TCS, two-component signal transduction system; UV, ultraviolet; WT, wildtype; XANES, X-ray absorption near-edge structure; XAS, X-ray absorption spectroscopy.

INTRODUCTION

Bacteria are robust microorganisms that are capable of surviving in numerous, diverse conditions due to their abilities to sense, to respond, and to adapt to dynamic environments.[1–5] Most bacteria utilize two-component signal transduction systems (TCSs) to mediate communication between extracellular and intracellular milieus in order to facilitate this adaptation.[6,7] TCSs are widespread among bacteria and regulate critical cellular processes like motility, chemotaxis, the production of virulence factors, and the acquisition of essential nutrients such as transition metals.[1-8] The most common type of TCSs are membrane-bound and canonically

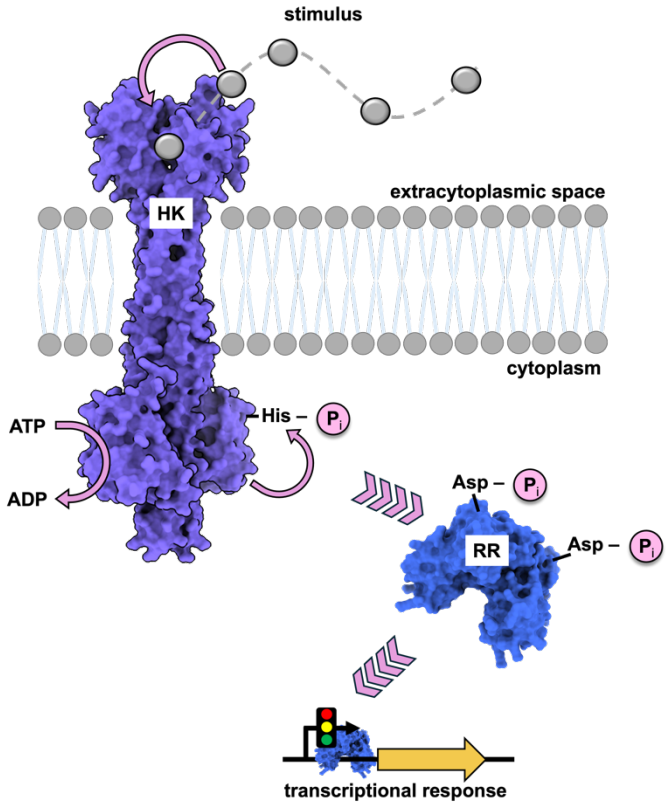

Figure 1. The signal transduction pathway of a canonical two-component system (TCS). Membrane-bound His kinases (HK) generally function as homodimers; when activated by an extracytoplasmic signal, the cytosolic kinase catalytic core of one HK monomer phosphorylates the same subunit of the neighboring dimer by transferring the γ-phosphate of ATP to the conserved His residue located in the dimerization and His phosphotransfer (DHp) domain. Upon the completion of this autophosphorylation event, the linked cytosolic response regulator (RR) accepts the transfer of the phosphate group to a conserved Asp within its N-terminal regulatory domain. As a result, the phosphorylated RR undergoes dynamical and conformational changes (generally dimerization) that modify the affinity of the RR to particular genes, ultimately leading to an altered transcriptional response.

combine two proteins to serve three functions: environmental recognition, signal transduction, and (most commonly) transcriptional regulation (Fig. 1). The two typical proteins comprising a TCS are the transmembrane sensor His kinase (HK) and the cytoplasmic response regulator (RR) (Fig. 1). The membrane-bound sensor HK receives the environmental stimulus by interacting directly with a signaling ligand, thus beginning the signal transduction process. Stimulus binding then induces HK autophosphorylation (HK-P_i),[9] after which the phosphate signal may be readily transferred to a conserved residue on the RR (RR-P_i) (Fig. 1).[9-11] Phosphorylation of the RR occurs at the N-terminal regulatory domain (site of a conserved Asp residue), triggering conformational and dynamical changes in the protein, altering the affinity of the RR to DNA and affecting transcriptional regulation (Fig. 1).[9, 12] Stimulus-specific HKs are generally paired with cognate RRs that activate or (less frequently) inhibit transcription of DNA when bound, thus regulating bacterial responses to external inputs.[9, 13-14] Since these systems facilitate the ability of bacteria to adapt to diverse environments, TCSs also function as critical virulence factors that enhance the infections of pathogens within hosts.[15-18]

One increasingly problematic pathogen that makes extensive use of TCSs to adapt to its host is *Pseudomonas aeruginosa*, a ubiquitous and opportunistic Gram-negative bacterium that can reside within virtually all environments and is most notably associated with nosocomial infections.[2,12] As one of the six multidrug-resistant ESKAPE pathogens, *P. aeruginosa* continues to be a global health threat and is well-known for infecting human patients such as those with burn wounds, neutropenia, and/or those suffering from cystic fibrosis (CF).[12] As part of its outstanding adaptability, *P. aeruginosa* can form biofilms, protective and intricate three-dimensional aggregates composed of polysaccharides, proteins, lipids, and DNA.[13–15] These complex structures enhance the ability of *P. aeruginosa* to cause infections and significantly decrease the immune

response of the host while increasing antibiotic resistance of the pathogen (≥ 1000-fold).[13,14] Moreover, *P. aeruginosa* may also employ numerous additional virulence factors that allow this infectious prokaryote to adapt to the environment of the host and to evade the immune system. Importantly, upon colonization, *P. aeruginosa* undertakes a transcriptional reprogramming in order to transition to a biofilm- and virulence factor-producing mode. This process is accomplished chiefly by TCSs that function to control the transcription of genes responsible for the formation and dispersal of biofilms as well as several essential virulence factors.[16–19]

One such critical TCS in *P. aeruginosa* is BqsRS, first discovered as a regulator of biofilm dispersal in PAO1,[20] then later found to sense extracellular Fe^{2+} and to promote resistance to cationic stress in PA14.[21] Also known as CarRS, the *Pa*BqsRS/CarRS TCS has also been reported to be highly induced by Ca^{2+}, to function as a regulator of Ca^{2+} homoeostasis, and to control Ca^{2+}-dependent pyocyanin production and tobramycin resistance.[22] *Pa*BqsRS is a canonical two-component system composed of a membrane-bound HK, BqsS, and its cognate RR, BqsR. Several lines of evidence have shown that the membrane HK *Pa*BqsS recognizes Fe^{2+} at μM metal concentrations as well as Ca^{2+} at mM concentrations, both of which are physiologically-relevant concentrations of metal cations within the lungs of CF patients.[23–28] Importantly, *P. aeruginosa* deletion mutants of *bqsS* and/or *bqsR* are defective in the production of short chain quorum sensing signals and rhamnolipids, glycolipid biosurfactants necessary to maintain biofilm architecture.[20] This BqsRS-mediated alteration in biofilm maintenance ultimately leads to biofilm dispersal that is commonly associated with the spread of infection, indicating that the BqsRS likely plays a critical regulatory role in *P. aeruginosa* virulence.[29] Furthermore, studies using the motif search program MEME[30] coupled with electrophoretic mobility shift assays (EMSAs) discovered that *Pa*BqsR binds within a tandem repeat DNA sequence 5'-TTAAG$(N)_6$-TTAAG-3' (also known as

the BqsR box).[21] This sequence is upstream of over 100 genes in *P. aeruginosa*, including those involved in metal transport, lipopolysaccharide modulation, polyamine synthesis and transport, and even antibiotic resistance, suggesting that this TCS could be a potential drug target and emphasizing the importance of investigating this system's structural properties, its regulated genes, and its mechanism of action.[21,31,32]

We have recently characterized intact and truncated *Pa*BqsS to understand its function and its mechanism of metal selectivity.[33] Specifically, we showed that intact, detergent-solubilized *Pa*BqsS functions as a homodimer and binds a single Fe^{2+} ion within a dimeric interface of the *Pa*BqsS periplasmic domain. X-ray absorption spectroscopy (XAS) and site-directed mutagenesis demonstrated that this Fe^{2+} ion was bound in an octahedral geometry and coordinated by two critical Glu residues, supporting previous transcriptomics data.[21] We then characterized the ATP hydrolysis of intact *Pa*BqsS and its truncated cytoplasmic domain, and we showed that intact *Pa*BqsS was selectively and exclusively stimulated by the binding of Fe^{2+} in its periplasmic sensor domain. This study was the first to characterize an intact HK bound to its cognate metal. However, many questions remained regarding the structure, the function, and the DNA-binding mechanism of the cognate RR of this system, *Pa*BqsR.

In this study, we have determined the structural and the functional properties of the intact, activated, and truncated forms of the *P. aeruginosa* response regulator BqsR. We have solved the X-ray crystal structure of the N-terminal *Pa*BqsR receiver domain to 1.3 Å resolution, we have determined the structure of the C-terminal *Pa*BqsR DNA-binding domain (DBD) using nuclear magnetic resonance (NMR), and we have modeled the *Pa*BqsR-DNA interactions using AlphaFold. Excitingly, we have found a *Pa*BqsR DNA-binding site upstream of the *feo* operon that encodes for the primary Fe^{2+} transport machinery in *P. aeruginosa*. Using *in vitro* DNA-

binding assays, we show that *Pa*BqsR can bind upstream of *feo* and within the BqsR box that overlaps the FUR box that regulates this operon in iron-replete conditions. Correlating with these *in vitro* observations, transcriptomic changes in Δ*bqsR* PAO1 show that *feo* is among the most differentially regulated genes by *Pa*BqsR, making *feo* one of the primary targets of this TCS. Moreover, we demonstrate that *Pa*BqsR regulation is dynamic and responds to Fe^{2+} availability in PAO1, likely through the ability of *Pa*BqsR to bind Fe^{2+} itself, which has not been observed in other OmpR-like response regulators, representing an additional layer of regulation in this system. Taken together, these data elucidate the structure and the DNA-binding properties of *Pa*BqsR for the first time, define its transcriptional regulon, and reveal an important and novel function for BqsRS in controlling *P. aeruginosa* Fe^{2+} acquisition.

RESULTS

The crystal structure of the N-terminal domain of PaBqsR reveals an OmpR/PhoB-like phospho-acceptor domain.

To determine the structural and biophysical properties of *P. aeruginosa* BqsR (*Pa*BqsR), we cloned, expressed, and purified the intact RR to homogeneity (Fig. S1a). At low concentrations (<< 1 mM), *Pa*BqsR migrated via gel filtration as a monomer, although at high concentrations (*ca.* 1 mM) this oligomerization shifted to a dimeric species (Fig. S1b), suggesting this protein is in dynamic equilibrium between monomer and dimer. Using both species of protein, we set up an extensive series of crystallization screens, optimized the obtained crystals, and tested for diffraction. All crystals indexed to the same space group, and our highest resolution was resolved to 1.3 Å (Table S1). However, a Matthew's analysis of the lattice parameters was inconsistent with the presence of intact *Pa*BqsR. Guided by sequence conservation amongst other similar RRs, we generated independent AlphaFold models of the N-terminal receiver and C-terminal DNA-binding domains (DBD) of *Pa*BqsR, and we used those as search models for molecular replacement (MR). The N-terminal receiver domain alone produced a definitive MR solution, whereas the C-terminal DBD did not. Subsequent refinement converged to a final model (R_w = 0.158, R_f = 0.175) in which only residues 1-123 (chiefly comprising the N-terminal receiver domain) are present (Table S1; PDB ID 8GC6). Despite exhaustive attempts to crystallize the intact, wildtype (WT) *Pa*BqsR protein, we were unable to do so, and all conditions produced crystals of the proteolyzed N-terminal receiver domain alone, likely due to the high dynamics in the linker region connecting this domain to the C-terminal DBD.[34]

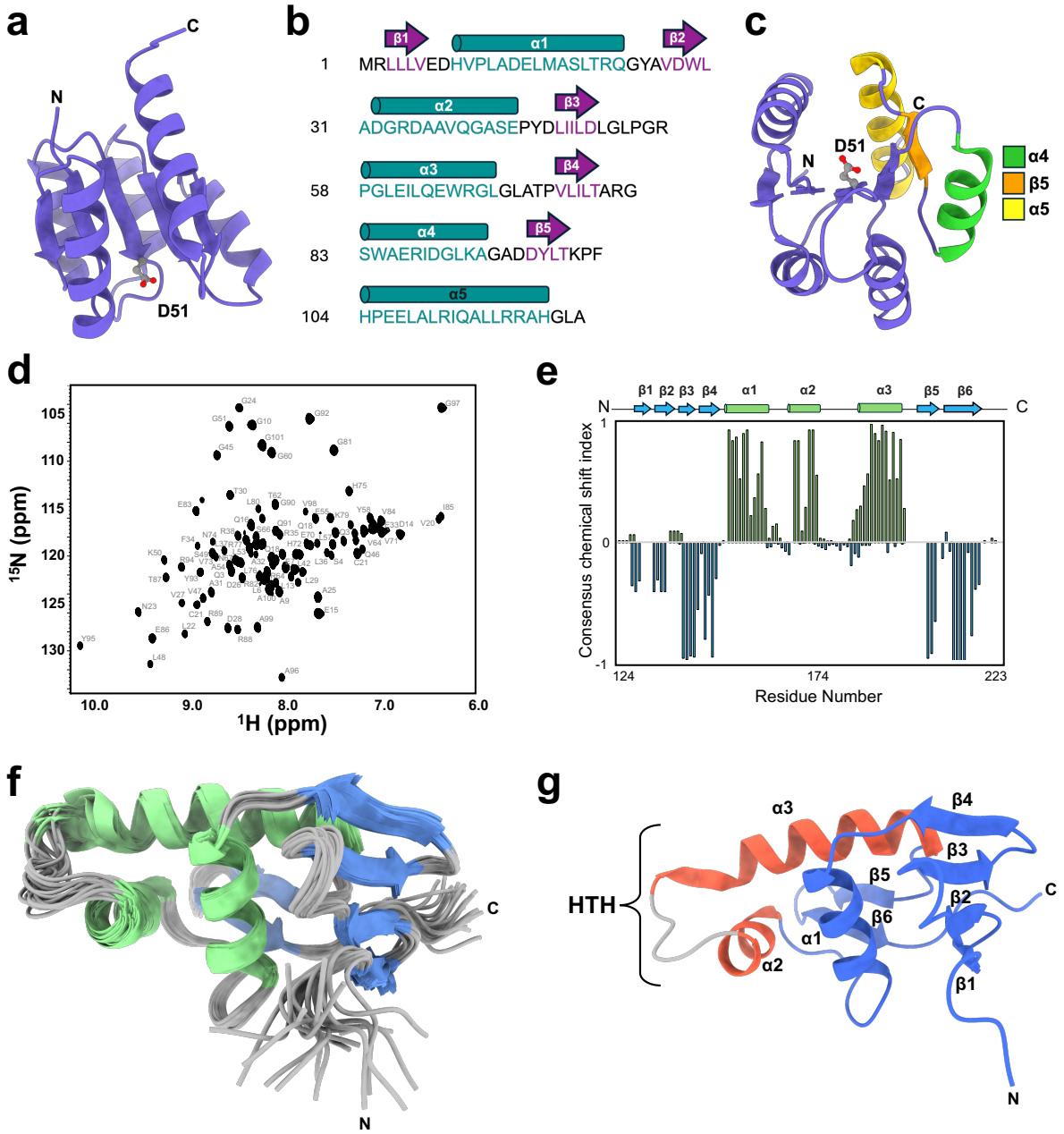

Figure 2. Structural analysis of *Pa*BqsR. **a**. The crystal structure of the *Pa*BqsR N-terminal receiver domain (residues 1-123) reveals an OmpR/PhoB family canonical $(\beta\alpha)_5$ response regulator assembly with a central five-stranded parallel β-sheet surrounded by five α-helices. **b**. Cartoon topology of the *Pa*BqsR N-terminal receiver domain. **c**. Dimer formation for OmpR/PhoB response regulators is generally mediated by the α4–β5–α5 interface, highlighted in green, orange, and yellow, respectively. **d**. Assigned 2D ^{1}H-^{15}N HSQC NMR spectrum of *Pa*BqsR DBD. **e**. Consensus chemical shift index (CSI) (Hα, Cα, and Cβ and C0) of *Pa*BqsR DBD, calculated using the program CSI 3.0.[35] Values nearing +1 indicate α-helical structure, values near 0 indicate unstructures regions/random coil, and values nearing -1 indicate β-strand structure.The cartoon at the top indicates the predicted toplogy of the *Pa*BqsR DBD based on CSI values derived from NMR experiments. **f**. Superpositioning of the 20 lowest-energy refined structures of the *Pa*BqsR DBD (residues 124-223). Labeled are the α-helices (green) and β-strands (blue). **g**. Ribbon diagram of the lowest-energy conformer of the *Pa*BqsR DBD, which contains a helix-turn-helix (HTH) topology common to the OmpR/PhoB-like family. The helix-turn-helix (HTH) motif that comprise the topology of the protein is labeled (red). In all cases, 'N' and 'C' represent the N- and C-termini in the structure, respectively.

The N-terminal *Pa*BqsR receiver domain has strong structural homology to phosphor-acceptor domains of the family of OmpR/PhoB-like RRs (Fig. 2a-c). In particular, our new structure reveals that *Pa*BqsR possesses a canonical $(\beta\alpha)_5$ response regulator assembly that consists of a central five-stranded parallel β-sheet surrounded by five α-helices (Fig. 2a,c). This topology is very common for the OmpR/PhoB-like family, and superpositioning reveals strong structural homology (Cα RMSDs < 1.0 Å) to other receiver domains found in bacterial RRs such as PhoP, ArlR, and KdpE (Fig. S2). One end of the receiver domain is highly negative in its electrostatic surface (likely driving interactions with its partner HK *Pa*BqsS), and the key, conserved phospho-accepting residue Asp^{51} stretches out to the surface of this part of the protein, likely to facilitate reaction with the phosphorylated HK to catalyze phospho-relay (Fig. 2a,c). In contrast, the dimerization of *Pa*BqsR is facilitated through a conserved dimerization domain comprising the α4–β5–α5 region (Fig. 2c) that is of mixed electrostatic polarity and ultimately links to the C-terminal DBD through a flexible linker. Unfortunately, in WT *Pa*BqsR, the dynamics of the flexible linker make this protein prone to spontaneous proteolysis over time in the crystallization drop, which could not be avoided despite numerous efforts. Thus, a different approach was needed to characterize the C-terminal DBD.

The C-terminal DNA-binding domain (DBD) of PaBqsR bears a helix-turn-helix (HTH) topology.

As we failed to crystallize the intact structure of *Pa*BqsR, we cloned, expressed, and purified to homogeneity a construct that consisted only of the C-terminal *Pa*BqsR DBD (Fig. S1a). Gel filtration experiments demonstrate that the DBD maintains a monomeric oligomerization at both low and high concentrations (Fig. S1b), in contrast with the WT protein but consistent with the dimerization domain being located in the *Pa*BqsR N-terminal domain. Despite exhaustive

attempts, we were unable to produce crystals with this protein. Therefore, we instead turned to nuclear magnetic resonance (NMR) to determine the structure of the DBD. We first collected high-quality 2D ^{1}H-^{15}N heteronuclear single quantum coherence (HSQC) spectra of the *Pa*BqsR DBD (Fig. 2d) that indicated folded protein based on its well-dispersed amide signals. We then tested several pH ranges to optimize the intensity of the ^{1}H and ^{15}N chemical shifts (pH 5.5 was found to be optimal), we confirmed that the protein was stable for several weeks at this pH, and we used 2D NMR data collected at this pH for backbone amide assignments. These established NMR conditions ultimately allowed for assignment of all backbone amide signals except Met^{1} (99 % of the non-proline backbone amide signals) (Fig. 2d).

To explore the secondary structure of the *Pa*BqsR DBD, Cα chemical shift indices (CSI) based on the assignment of triple resonance spectra were analyzed (Fig 2e), indicating that the secondary structure of the DBD is composed of a N-terminal set of 4 β-strands (β1, Leu^{128}–Ala^{131}; β2, Leu^{133}–Leu^{135}; β3, Cys^{141}–Leu^{144}; β4, Ala^{147}–Asp^{150}) followed by three α-helices (α1, Ala^{153}–Met^{163}; α2, Lys^{172}–Leu^{179}; α3, Glu^{185}–Leu^{202}). The DBD then terminates with two β-strands (β5, Ile^{207}–Arg^{210}; β6, Gly^{214}–Tyr^{217}) suggesting the presence of a short β-hairpin, a structural feature in DBDs that has been shown to be important in facilitating the interaction between bacterial RRs (such as PhoP, ArlR, and KdpE) and their DNA targets.[35–39] In order to confirm this architecture, the tertiary structure of the *Pa*BqsR DBD was determined by preparing ^{15}N- and ^{15}N/^{13}C-isotopically enriched protein sample and acquiring 3D ^{15}N-edited nuclear Overhauser effect (NOE) spectra.[40,41] After data acquisition, structural calculations were carried out using a total of 1912 interproton distance restraints derived from NOE data, 48 hydrogen bond restraints, and 148 dihedral restraints based on backbone chemical shifts (Table S2). An ensemble of 20 refined *Pa*BqsR DBD structures was ultimately generated that exhibited good convergence based on root-

mean-square deviations (RMSDs) (0.93 Å ± 0.11 Å for backbone heavy atoms) (Fig. 2f, Table S2) (PDB ID 9FYA).

The tertiary structure of the *Pa*BqsR C-terminal DBD is wholly consistent with the CSI analysis and displays a helix-turn-helix (HTH) DNA-binding topology common to the OmpR/PhoB RR family (Fig 2e-g). The N-terminal β-sheet interacts with helix α1 through hydrophobic interactions while π-stacking interactions between the aromatic rings of Phe162 and Tyr215 bring the N-terminal β-sheet in proximity to the C-terminus. The three α-helices (α1-α3) form the trihelical motif of the HTH, with α3 representing the longest and most polar helix that interacts with the DNA major groove (*vide infra*). This overall HTH fold is common to the DBDs of the OmpR/PhoB RR family, and structural superpositioning reveals strong structural homology (Cα RMSDs < 1.3 Å) to other DBDs found in bacterial RRs such as PhoP, ArlR, and KdpE (Fig. S3).[35–39] Additionally, the *Pa*BqsR C-terminal DBD ends in a critical β-hairpin that has been shown in other RR DBDs to be important in DNA binding (*vide infra*).[35–39] However, subtle differences in the DNA-binding helices and this key β-hairpin generally drive specificity and differentiate the gene targets of these RRs, which we then explored.

In vitro DNA-binding assays reveal that PaBqsR binds upstream of the feo operon in PAO1.

As we previously demonstrated that the sensor HK of the BqsRS system, *Pa*BqsS, binds and forms a stable interaction with Fe^{2+},[33] we hypothesized that one (or several) of the gene targets of this TCS would be involved in iron homeostasis, an essential component for bacterial survival and a critical factor in biofilm formation and virulence of *P. aeruginosa*.[29,42,43] Prior work defined the BqsR box sequence as 5'-TTAAG$(N)_6$-TTAAG-3'[21], so we first undertook a directed search of a limited portion of the PAO1 genome for this DNA sequence, searching for its presence upstream of genes of interest such as those involved in spermidine synthesis,[44] Fe^{3+} reduction,[45,46]

and Fe^{2+} acquisition[47] (Table S3). Given that *Pa*BqsR can sense Fe^{2+} directly, we were particularly interested in whether *Pa*BqsR could target the *feo* operon that encodes for the primary Fe^{2+} transport machinery in PAO1. Interestingly, we observe a putative BqsR box upstream of the PAO1 *feoA* start site, overlapping with a putative ferric uptake regulator (FUR) box (a global, negative iron regulator), but distal from, and independent of, a putative anaerobic transcriptional regulator (ANR) box (a global regulator of anaerobic genes) (Fig. 3a). These results suggested that *Pa*BqsR could regulate *feo* expression in PAO1, which we then tested *in vitro*.

To determine whether *Pa*BqsR could bind to the BqsR box upstream of the *feo* operon, we used *in vitro* electrophoretic mobility shift assays (EMSAs). To do so, we tested binding using a 21 base-pair (bp) DNA duplex corresponding to minimal region needed for protein binding (Table

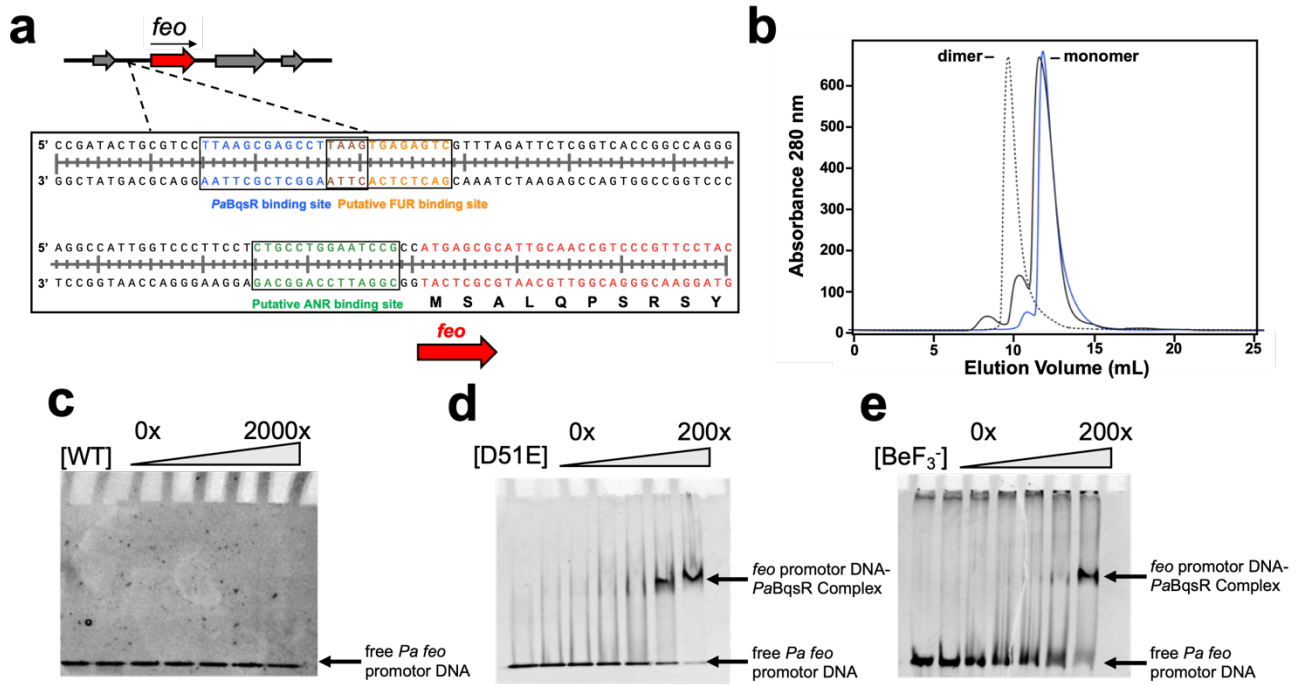

Figure 3. *Pa*BqsR binds upstream of the *feo* operon in PAO1. **a**. A putative BqsR box sequence (5'-TTAAG(N)$_6$-TTAAG-3'; blue) is present in PAO1 upstream of *feo*, overlaps with a putative ferric uptake regulator (FUR) box (orange), and is upstream of the anaerobic transcriptional regulator (ANR) box (green), adjacent to the start site of the *feo* operon (red). **b**. Size exclusion chromatography (SEC) profiles of WT *Pa*BqsR (black), D51E *Pa*BqsR (blue), and BeF_3^--activated *Pa*BqsR (dashed). BeF_3^--activated *Pa*BqsR is a dimer, while WT and D51E *Pa*BqsR are both monomers at low concentrations (<< 1 mM). **c**. EMSAs with WT *Pa*BqsR and the *feo* duplex. **d**. EMSAs with D51E *Pa*BqsR and the *feo* duplex. **e**. EMSAs with the BeF_3^--activated *Pa*BqsR and the *feo* duplex.

S4). Intact, monomeric, WT *Pa*BqsR (Fig. 3b) failed to bind to this duplex when tested across a range of concentrations from 0-2000 mol. eq. protein:DNA (Fig. 3c). This behavior was expected, as the canonical TCS paradigm indicates that the RR must either be phosphorylated or pseudo-phosphorylated to facilitate DNA binding.[7] As RR pseudo-phosphorylation can be achieved by producing an Asp-to-Glu variant in which alteration in length of the phosphorylatable Asp residue results in RR activation, or by reaction with BeF_3^- that binds to the phosphorylatable Asp residue in the RR and mimics the presence of a phosphate group, we tested both approaches. We first used mutagenesis to create a *Pa*BqsR D51E variant that we expressed and purified to homogeneity (Figs. 3b, S1b). Interestingly, while this protein remained monomeric in solution (Figs. 3b, S1b), the D51E variant showed clear and distinct binding to the *feo* duplex (Fig. 3d), demonstrating that protein dimerization in the absence of DNA is not a pre-requisite for intact *Pa*BqsR to bind to DNA, and that pseudo-phosphorylation enhances the *Pa*BqsR-DNA interaction. We then generated the pseudo-phosphorylated, WT BeF_3^--activated form of *Pa*BqsR that was clearly dimeric in solution (Figs. 3b, S1b). The BeF_3^--activated phospho-mimetic of *Pa*BqsR also bound to the *feo* duplex with an apparent affinity nearly identical to the D51E variant (Fig. 4e). Control EMSAs using bovine serum albumin (BSA) in place of *Pa*BqsR failed to bind to the *feo* duplex, demonstrating this interaction to be *Pa*BqsR-specific (Fig. S4). Finally, we tested whether the monomeric *Pa*BqsR C-terminal DBD alone could bind to DNA. Indeed, we observed binding to the *feo* duplex with only the DBD (Fig. S4), but the apparent binding was 2-3 fold weaker than that of either D51E or the BeF_3^--activated form of full-length *Pa*BqsR (Fig. S4), indicating that the presence of the N-terminal receiver domain contributes to the binding affinity of this RR to its DNA sequence. Taken together, these results demonstrate that *Pa*BqsR may target the *feo*

upstream region *in vitro*, suggesting that this TCS is a regulator of a critical iron uptake system frequently used by *P. aeruginosa* at the host-pathogen interface.[48]

Modeling of PaBqsR and the PAO1 feo operon illustrates a unique mode of DNA binding.

We next sought to use structural approaches to understand how *Pa*BqsR binds to the upstream *feo* region. To do so, we first tried to crystallize both *Pa*BqsR D51E and the BeF_3^--activated forms of *Pa*BqsR in the presence of the *feo* upstream region duplex modified to include an additional G-C overhang, which has been shown to increase crystallization propensity of other DNA-protein complexes.[49] While we were able to generate crystals of both complexes, these crystals only diffracted weakly and anisotropically despite extensive optimization. We then turned to AlphaFold to model the *Pa*BqsR-*feo* interaction (Fig. 4a), as we already possessed experimentally-determined structural information on both domains of *Pa*BqsR. Surprisingly, there is little consensus on how exactly OmpR/PhoB-like RRs recognize and bind to their target DNA sequences. For example, the DBDs of PhoB, PmrA, or RstA bind DNA asymmetrically,[35,37,39] whereas the DBD of OmpR binds to various DNA sequences in either a symmetric or asymmetric orientation,[36,50,51] further underscoring the importance of investigating the *Pa*BqsR DNA binding. Consistent with the behavior of the BeF_3^--activated form of WT *Pa*BqsR, AlphaFold predicts binding of *Pa*BqsR to the *feo* upstream region as a dimer (Fig. 4a), as no binding is predicted when only a single copy of *Pa*BqsR is provided as an input. Intriguingly, modeling predicts that dimerization at the N-terminal phospho-acceptor domain occurs in an asymmetric manner, and this dimerization orientation may be facilitated by the phosphorylation of Asp^{51} (Fig. 4a). Importantly, as predicted based on NMR data (Fig. 2), α3 of the HTH motif of the C-terminal DBD

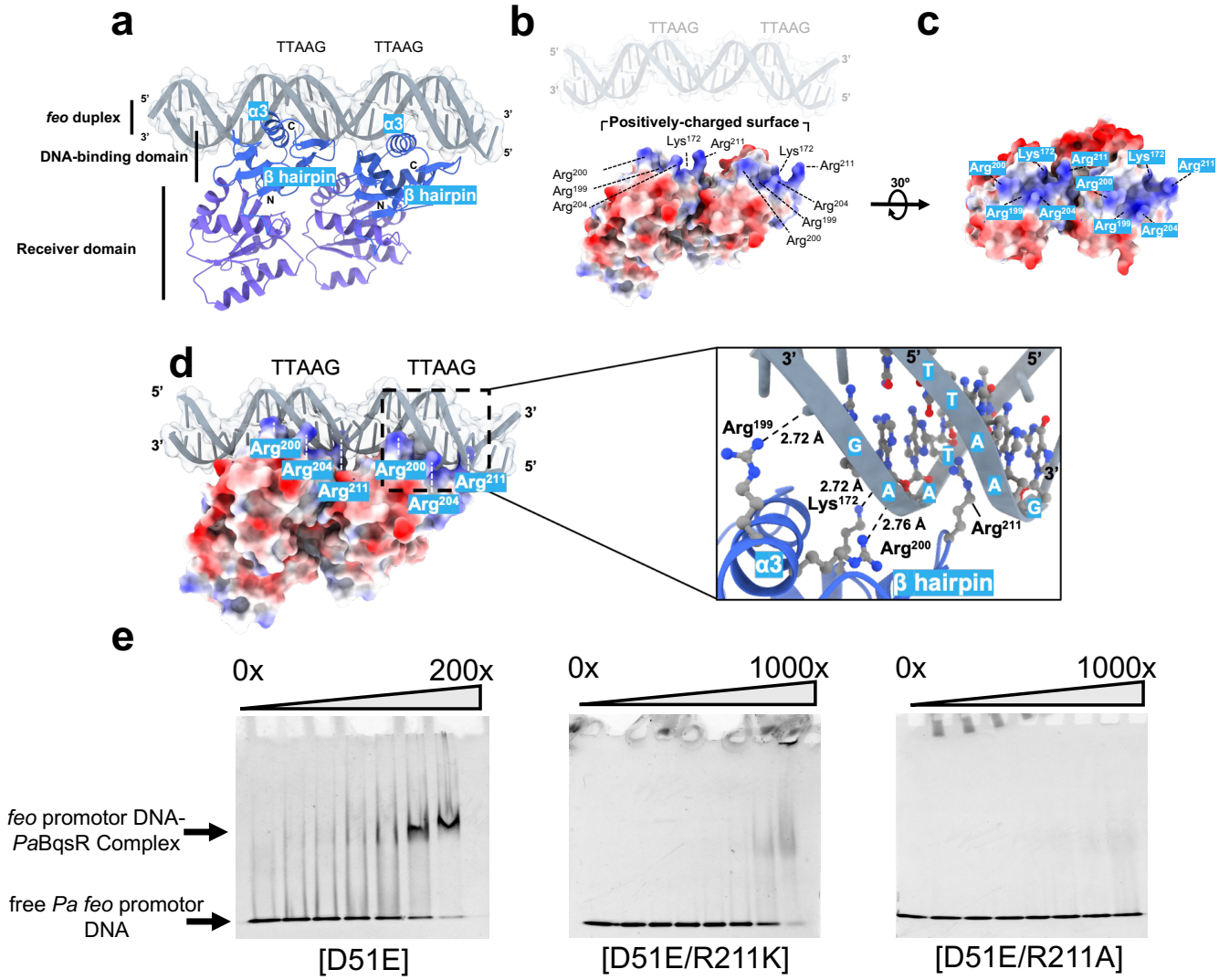

Figure 4. Modeling of *Pa*BqsR binding to the *feo* duplex. **a**. AlphaFold model of WT, intact *Pa*BqsR bound to the *feo* upstream duplex. The region in purple is the N-terminal receiver domain, while the region in blue is the C-terminal DNA-binding domain (DBD). **b,c**. An electrostatic surface comprising Lys^{172}, His^{194}, His^{197}, Arg^{199}, Arg^{200}, and Arg^{204} extends across the dimer and utilizes the exposed α3 of each *Pa*BqsR monomer to bind within the DNA major groove. **d**. Lys^{172}, Arg^{199}, Arg^{200}, and Arg^{211} directly interact with the BqsR box, with residue Arg^{211} forming an anchor that π-stacks into each half of the tandem repeat, providing specificity. In all cases, 'N' and 'C' represent the N- and C-termini in the structure, respectively. **e**. EMSAs of *Pa*BqsR variants (D51E, D51E/R211K, D51E/R211A) in complex with the PAO1 *feo* upstream region indicates that the D51E/R211K variant has a lowered affinity to the PAO1 *feo* upstream region, while the D51E/R211A variant fails to bind to the PAO1 *feo* upstream region at the same ratio.

binds within the major groove of DNA (Fig. 4a) but within the variable nucleotide region and upstream (towards the 5' end of the sense strand) of the conserved 5'-TTAAG-3' sequence (Fig. 4a). Basic residues of *Pa*BqsR such as Lys^{172}, His^{194}, His^{197}, Arg^{199}, Arg^{200}, and Arg^{204} create a positively-charged surface that includes the exposed face of α3 on each *Pa*BqsR protomer and

extends across the dimer (Fig. 4a-c). This important region contacts the DNA backbone and helps place α3 into the major groove of the DNA (Fig. 4b-d) with the sidechains of Lys^{172}, Arg^{199}, and Arg^{200} making contact tightly with the DNA phosphates (with the closest sidechain-phosphate distances of 2.72 Å, 2.72 Å, and 2.76 Å, respectively) (Fig. 4d, inset). Additionally, the terminating β-hairpin of each dimer contains Arg^{211}, an "anchoring" Arg residue that makes direct contacts with the BqsR box through three specific nucleobases of the tandem repeat: Arg^{211} on the first protomer hydrogen bonds with T^{33} and A^{34} on the sense strand and A^{24} on the antisense strand, while Arg^{211} on the second protomer hydrogen bonds with A^{36} on the sense strand and T^{22} and A^{23} on the antisense strand (Fig. 4d, inset). Thus, modeling suggests that at least 7 different amino acids in the DBD facilitate contacts between each *Pa*BqsR and DNA, with Lys^{172}, Arg^{199}, Arg^{200}, and Arg^{211} likely playing the most important roles in recognizing the BqsR box.

To understand whether the intercalating β-hairpin residues are conserved across OmpR-like RRs, and to test the hypothesis that Arg^{211} "anchors" the RR to the *feo* upstream region, we used bioinformatics, site-directed mutagenesis, and EMSAs. Several biochemically-characterized RRs conserve the HTH and β-hairpin structural motifs while having poor sequence conservation (Figs. S5), suggesting that it is not sequence alone that determines DNA-binding. Interestingly, Arg^{211} in the *Pa*BqsR DBD is poorly conserved across OmpR-like RRs (Fig. S5), so to test the importance of Arg^{211} in mediating protein-DNA interactions, we expressed, purified, and tested for DNA binding several *Pa*BqsR variants (Fig. S6): R211A (does not dimerize but abrogates the positively-charged locus in this position), R211K (does not dimerize but maintains the positively-charged locus in this position), D51E/R211A (mimics activation but abrogates the positively-charged locus in this position), and D51E/R211K (mimics activation and maintains the positively-charged locus in this position). As expected, the inactivated R211A and R211K variants failed to

bind to the *feo* upstream region. In contrast, for the pseudo-activated D51E/R211K variant, EMSAS showed that binding still occurs, albeit weaker (> 5-fold) compared to the D51E variant alone (Fig. 4e). Finally, in the pseudo-activated D51E/R211A variant, removal of the charge in this position eliminated binding (Fig. 4e). These data reveal that it is not charge alone in this position that drives *Pa*BqsR-DNA interactions, but the planar guandinium moiety is crucial to maintain binding strength. These data provide support for our calculated model (Fig. 4a-d) and reveal that this terminating β-hairpin Arg^{211} "anchors" *Pa*BqsR to the BqsR box.

PaBqsR regulates a substantial portion of the PAO1 genome, including the feo operon.

To determine the *in vivo* regulatory impact of BqsR in *P. aeruginosa*, we conducted an RNA-seq analysis comparing the transcriptomes of wild type (WT) PAO1 and an isogenic Δ*bqsR* mutant (PRJNA874094). For this experiment, total RNA was isolated from both strains grown aerobically to mid-log phase (12 h) in biofilm minimal 8 (BMM8.5; see Methods) with an added sufficient concentration of iron (4 μM $FeSO_4$). Differential expression analysis revealed that BqsR regulates approximately 43 % of the PAO1 transcriptome, with 1311 genes significantly upregulated (log_2-fold change (LFC) ≥1, $p < 0.05$) and 1128 genes significantly downregulated (LFC ≤ -1, $p < 0.05$), indicating that the protein functions as both an activator and repressor of gene expression in *P. aeruginosa* (Fig. 5a). This vast array of regulation significantly expands on the previously reported regulatory role of the protein in response to Ca^{2+} addition[22] and Fe^{2+} shock during anaerobic growth,[21,31] revealing that BqsR is a global regulator of gene expression in *P. aeruginosa*. The ability of *Pa*BqsR to act as both a positive and negative transcriptional regulator is not unprecedented, as several other RRs have been reported to have a dual mode of

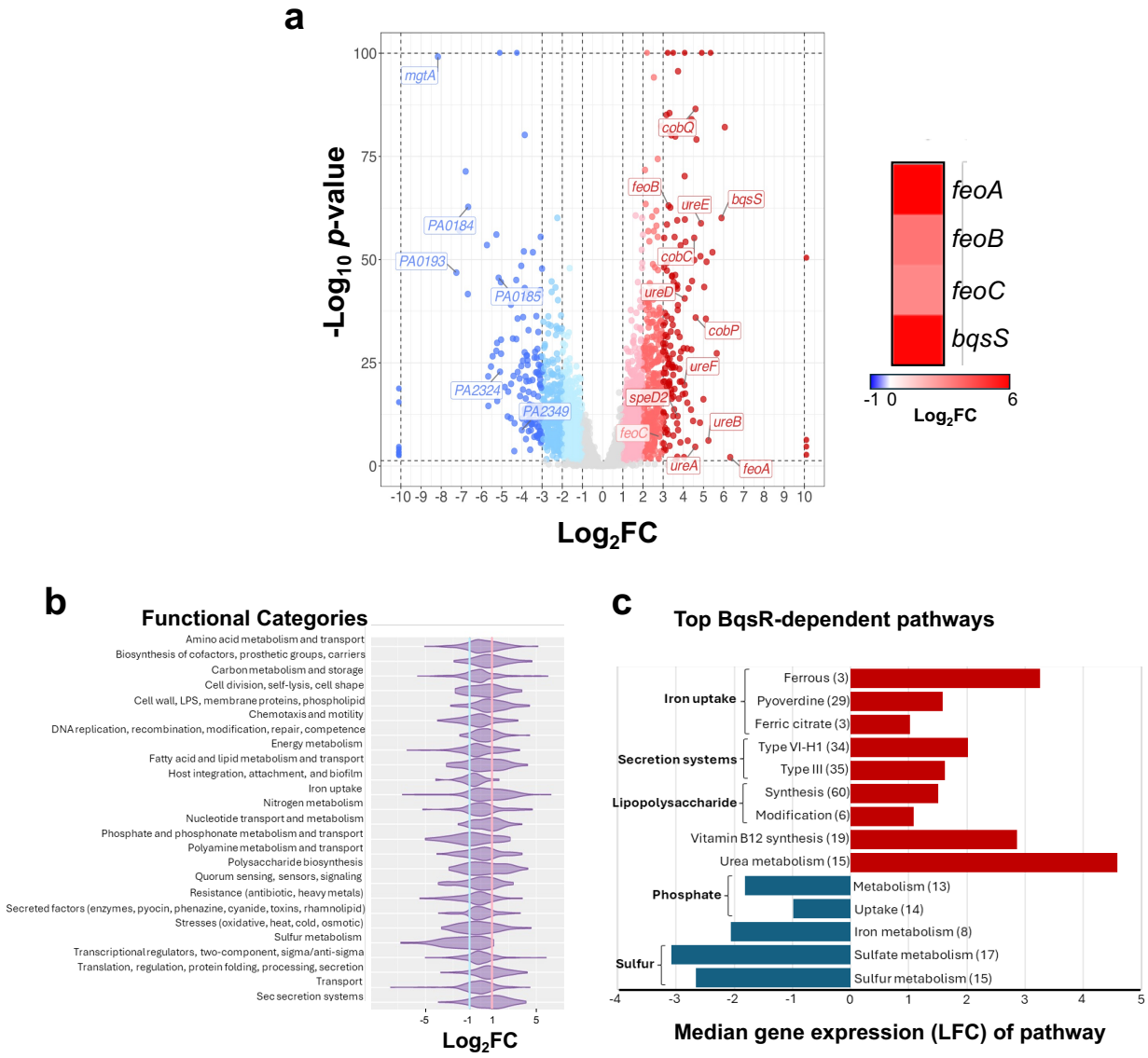

Figure 5. BqsR regulates a significant portion of the PAO1 genome. **a**. Volcano plot depicting the differentially expressed genes (DEGs) in Δ*bqsR* vs PAO1. DEGs ($Log_2FC \geq |1|$, $p < 0.05$) were stratified based on their $\log_2$ fold change (LFC) into three categories: low response with the expression changed by LFC |1-2| (light red/blue); moderate response with LFC |2-3| (medium red/blue); and top responders with LFC ≥ |3| (dark red/blue). Genes that showed no change in expression are shown in gray. False discovery rate (*p*-value) is plotted as $-Log_{10}$ *p*-value with a cutoff of 1.3 ($p = 0.05$) indicated by a horizontal dashed line. Genes with LFCs ≥ 10 and/or $-\log_{10}p$-values ≥ 100 are depicted along the outermost dashed lines for a clear visual. Genes encoding the most significantly altered pathways are labeled with their gene name or PA number (as annotated in pseudomonas.com). RNAseq-based heat map showing LFC of expression comparisons of *feoABC* and *bqsS* in Δ*bqsR* vs WT PAO1 (*inset*). Graph was generated in RStudio. **b**. Violin plots showing the functional categories impacted by BqsR in PAO1. The PAO1 functional categories were assigned based on hand-curated analysis. The vertical lines indicate the LFC 1 (red) and -1 (blue). **c**. The top BqsR-dependent pathways within the top differently regulated functional categories shown in **b**.

regulation.[18,52–54] However, previous research has implied that *Pa*BqsR acts only as a classical transcriptional activator when phosphorylated.[21]

To understand this large response more clearly, we stratified the differentially regulated genes into three categories: low responders in which the expression was altered between |1| ≤ LFC ≤ |2|, including 1527 genes; moderate responders in which the expression was altered between |2| ≤ LFC ≤ |3|, including 616 genes; and 296 top responders in which the expression was altered with a LFC ≥ |3|. To evaluate whether the moderate and top responders were direct targets of *Pa*BqsR, we examined the correlation between the magnitude of differential expression and the presence of the *Pa*BqsR consensus binding sequence, termed the BqsR box, previously identified in PA14 (*vide supra*).[21] For this, we performed a full analysis of the PAO1 genome using the FIMO motif search within the MEME suite.[18] This analysis identified 103 genes containing the consensus sequence within their putative promoter regions, with only five genes possessing the *Pa*BqsR-box tandem consensus sequence identical to 5'-TAAG$(N)_6$-TTAAG-3'. The 103 identified genes showed LFC values ranging from -5.0 to 6.3 and included 50 genes not affected by the deletion under the tested conditions, indicating that direct regulation by *Pa*BqsR may be subtle, that *Pa*BqsR regulation may depend on additional interacting regulators and environmental cues, and that the *Pa*BqsR regulon extends beyond the genes detected in this experiment, further underscoring its role as a global regulator. To understand better the basis of positive and negative regulation by *Pa*BqsR, we selected a subset of genes that were either induced or repressed by *Pa*BqsR and analyzed the relative positions of the BqsR box and the predicted -10/-35 promoter sequences indicated by DeNovoDNA (Fig. S7). The analysis showed that the BqsR box was located downstream of the -10/-35 promoter sequences for the genes positively regulated by *Pa*BqsR (Fig. S7), whereas the genes with negative or both types of *Pa*BqsR regulation showed the BqsR box overlapping with at least one of the -10/-35 regions (Fig. S7). Although based on a small set of genes, these observations suggest that the position of the BqsR box relative to the

predicted promoter provides a basis for two distinct regulatory outcomes of *Pa*BqsR activity and indicates that *Pa*BqsR may act in concert with other transcriptional factors or regulators, such as FUR and ANR, bindings site for both of which are also upstream of the *feo* operon.

To identify *Pa*BqsR-regulated processes and to evaluate the biological significance of this regulation, differentially expressed genes were sorted into general functional categories. These categories were assigned based on hand-curated gene annotation (see Methods). Interestingly, Fig. 5b shows that every functional category contained genes regulated by *Pa*BqsR. As evaluated based on both the magnitude of expression changes and the number of differentially expressed genes, the most significantly affected processes included iron uptake, phosphate metabolism, sulfur metabolism, and various transport systems. Among them, genes encoding iron sequestration (Feo, Pvd, and Fec), bacterial secretion systems (Type III and Type IV), lipopolysaccharide synthesis and modification, vitamin B_{12} synthesis, and urea metabolism were upregulated, whereas genes encoding phosphate and sulfur metabolism and uptake were downregulated in the absence of *bqsR* (Fig. 5c).

One of the most strongly responding pathways regulated by *Pa*BqsR was Fe^{2+} transport encoded by the *feo* operon. While we predicted that BqsR would regulate *feo* based on our *in vitro* results (Fig. 4), we were surprised that our RNA-seq results revealed that expression of *feoA*, *feoB*, and *feoC* was significantly increased (LFC of 6.3, 3.3, and 2.8, respectively) in the Δ*bqsR* mutant (Fig. 5a, inset). This elevated expression of *feoABC* in the absence of BqsR suggests that the protein negatively regulates the *feo* operon in PAO1 grown aerobically with a low but sufficient iron level (4 μM). Further, deletion of *bqsR* resulted in a strong upregulation of its cognate sensor, *bqsS* (LFC of 5.8; Fig. 5a, inset). This observation is consistent with previous findings in PA14, where BqsR was shown to autoregulate its own expression;[31] however, in that study, self-

regulation of *bqs* was observed to be positive when PA14 was grown under anaerobic conditions in the presence of shocking levels (100 μM) of Fe^{2+}. Together, these findings identify a relatively large regulon of *Pa*BqsR and indicate that this TCS has a major role in conditional control of Fe^{2+} acquisition, but the type of regulation initially observed was counter to our expectations.

PaBqsR regulation is dynamic and responds to Fe^{2+} availability.

While we expected that our RNA-seq data would reveal that the *feo* operon was among the top differentially expressed genes regulated by *Pa*BqsR, we were initially surprised that regulation appeared to be negative at low but sufficient levels of Fe^{2+} (4 μM). Since RNA was isolated from aerobic cultures, we hypothesized that levels of Fe^{2+} during growth may fluctuate, affecting the output of Fe^{2+}-dependent *feo* regulation. To investigate the relationship between Fe^{2+} availability and *feo* expression, we constructed a *feo* promoter (P^{feo})-fusion luminescent chromosomal reporter by cloning a 300-bp DNA fragment upstream of *feoA* immediately prior to the start of the *lux* operon in pCTX-1-*lux* and tested its activity in tandem with growth studies. For this set of experiments, the WT and Δ*bqsR* strains harboring the reporter were grown in BMM8.5 containing 4 μM Fe^{2+} for 6 h and induced with low (4 μM) or high (100 μM) levels of Fe^{2+} (Fig. 6a,b). The iron stocks were prepared in the presence of ascorbic acid (AA) to minimize oxidation and therefore AA in the absence of Fe^{2+} alone served as a control. Prior to Fe^{2+} treatment (0-6 h), the levels of P^{feo}-driven *lux* expression increased over time with no significant difference between the WT and Δ*bqsR* strains (Fig. 6a). Based on growth and P^{feo}-*lux* expression profiles, we stratified the response into two phases (I and II). When exposed to 4 μM Fe^{2+}, a modest decrease in P^{feo}-*lux* expression in the Δ*bqsR* strain compared to the WT strain was observed during phase I (8-12 h), indicating a positive mode of *Pa*BqsR regulation. No difference in growth was observed at this

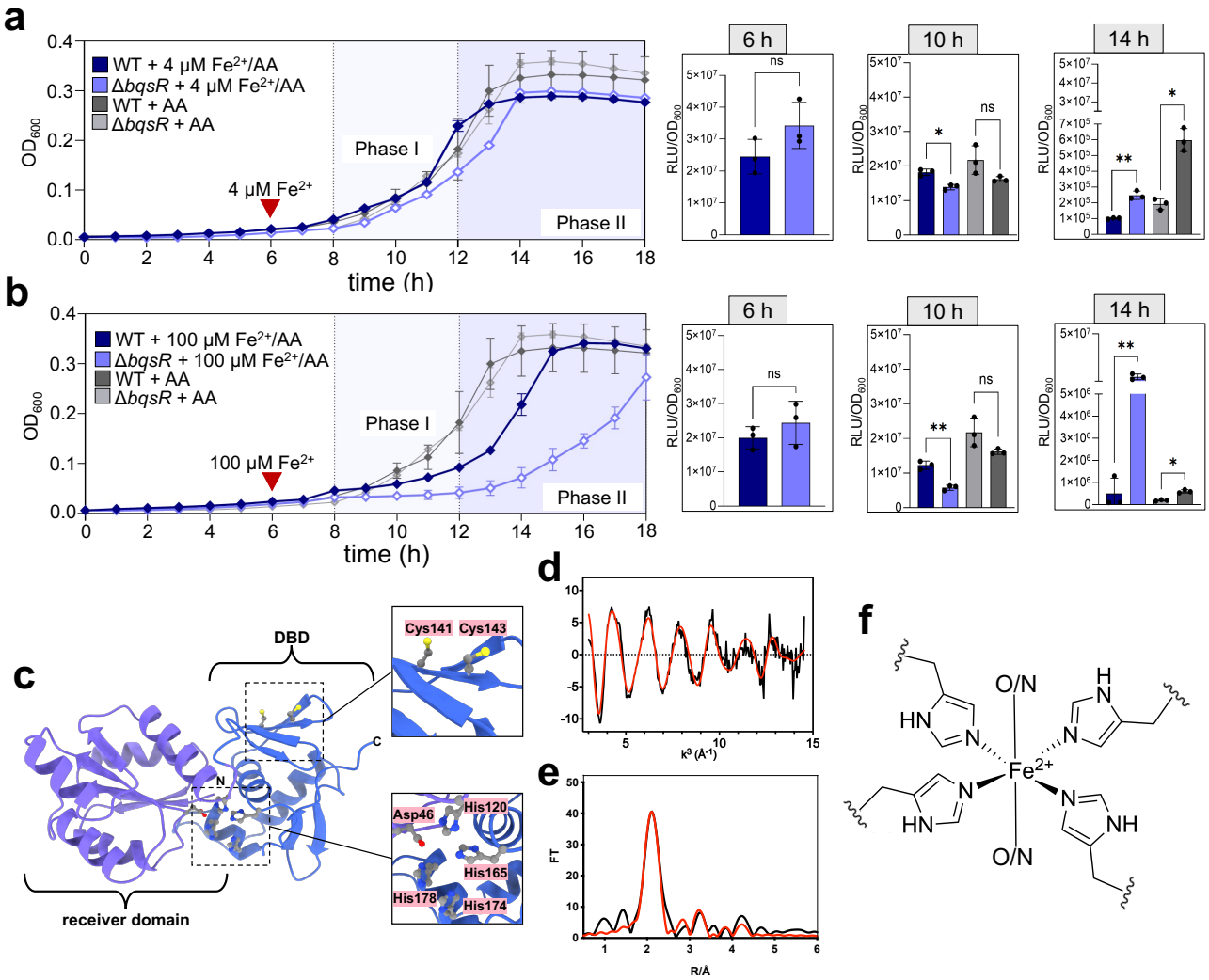

Figure 6. The *Pa*BqsR-mediated regulation of PAO1 growth and *feo* expression is dynamic and is likely controlled by Fe^{2+} availability. PAO1 strains harboring the chromosomal P^{feo}-*lux* fusion construct were grown in BMM8.5 containing 4 μM Fe^{2+}. After the first 6 h of growth, strains were exposed to 4 μM (**a**) or 100 μM (**b**) $FeSO_4$ prepared in 1 mM ascorbic acid (to prevent Fe^{2+} oxidation) or only 1 mM ascorbic acid (AA) without Fe^{2+} as a control. Optical density (OD_{600}) and relative luminescence units (RLU) were measured hourly. RLU were normalized to OD_{600}. The response was stratified into phases based on growth and expression profiles. Phase I (8-12 h) reflects a lag phase with a slight increase in growth; phase II (12-18 h) reflects exponential transitioning into stationary phase growth. Selected time-points representing the P^{feo}-*lux* expression profile within each phase include 6 h, 10 h, and 14 h are shown. Bars indicate the standard deviation of three independent biological replicates. Statistical significance was determined using the student's t-test. ** indicates $p \leq 0.01$. **c**. AlphaFold model of intact, WT *Pa*BqsR. Highlighted are the His-rich region at the interface of the two domains (*bottom right*) and the Cys-rich region (CxC motif; *top right*) in the DBD. **d**,**e**. EXAFS of *Pa*BqsR bound to Fe^{2+} under anoxic conditions. The processed EXAFS (**d**) and the resulting Fourier transformed data (**e**) are consistent with the presence of Fe^{2+} in a His-rich, octahedral geometry. The black traces represent the experimental data, while the red traces represent the EXCURVE-fitted data. **f**. Cartoon representation of the proposed Fe^{2+} coordination of *Pa*BqsR. 'N' and 'C' represent the N- and C-termini in the structure, respectively.

point. However, in the following phase II (12-18 h), P^{feo}-*lux* expression increased significantly in the Δ*bqsR* strain compared to the WT, suggesting a switch to negative regulation of *feo* expression by *Pa*BqsR (Fig. 6a). This increased expression coincided with a slight growth delay of the Δ*bqsR*

strain, suggesting that enhanced uptake of Fe^{2+} may lead to mild iron toxicity, which is quickly mitigated as growth returns to WT levels. The exposure to 100 μM Fe^{2+} resulted in a similar but more pronounced response. During phase I, P^{feo}-*lux* expression in the Δ*bqsR* strain was reduced compared to the WT (Fig. 6b), indicating a positive regulatory role of *Pa*BqsR in *feo* expression. This increased expression coincided with a slight reduction in WT growth and an even greater reduction in the Δ*bqsR* strain growth. During phase II, P^{feo}-*lux* expression in the WT decreased significantly relative to phase I, consistent with a *Pa*BqsR-mediated repression of *feo*. Supporting this observation, P^{feo}-*lux* expression in Δ*bqsR* increased dramatically compared to the WT (Fig.6b). These transcriptional changes coincided with a *ca*. 2 h growth delay in the WT strain and a longer delay (*ca*. 5 h) with slower growth in the Δ*bqsR* strain, likely due to the mutant's inability to repress *feo* expression leading to Fe^{2+} toxicity. To confirm that these effects were not reporter-dependent, we assessed the growth of PAO1 and Δ*bqsR* lacking P^{feo}-*lux* transcriptional fusion under the same conditions, which showed similar patterns upon exposure to low and high levels of Fe^{2+} (Fig. S8).

Motivated by these findings, we then tested whether *Pa*BqsR might bind Fe^{2+} directly, which could explain our *in vivo* findings that *Pa*BqsR regulation changes based on Fe^{2+} availability. In our structural characterization of the various domains of *Pa*BqsR (*vide supra*), we noted two regions of the protein conspicuously rich in potential iron-binding residues (a CxC motif in the DBD and a His-rich motif at the domain-domain interface; Fig. 6c), so we tested whether intact, WT *Pa*BqsR could bind Fe^{2+} like that of its HK counterpart, *Pa*BqsS.[33] Intriguingly, we observed stable binding of a single Fe^{2+} ion to WT *Pa*BqsR after anoxic loading and copious buffer exchanges, as confirmed by ferrozine assays and ICP-MS (Fig. S9). To characterize the identity and local structure of the Fe^{2+} ion bound to WT *Pa*BqsR, we then used X-ray absorption

spectroscopy (XAS). The energy of the inflection of the X-ray absorption near-edge structure (XANES) spectrum of Fe^{2+}-bound WT *Pa*BqsR as well as its lack of pre-edge features are consistent with an octahedrally-coordinated Fe^{2+} ion (Fig. S10). Simulations of the extended X-ray absorption fine structure (EXAFS) data of *Pa*BqsR (Fig. 6f) reveal only N/O-based environments surrounding the Fe^{2+} ion (Fig. 7d), with 4 ligands best fitted to His residues at 2.09 Å from the Fe^{2+} ion, while 2 ligands (perhaps water) are coordinated more weakly and are observed at 2.17 Å from the Fe^{2+} ion (Table S5). These data definitively rule out coordination of Fe^{2+} at the CxC motif in the C-terminal binding domain and strongly suggest that the His-rich region at the interface of the two domains in *Pa*BqsR (comprising His^{119}, His^{164}, His^{174}, His^{178}) binds the Fe^{2+} ion. Consistent with these notions, anoxic Fe^{2+} loading with just the C-terminal DBD of *Pa*BqsR failed to show any metal binding. To our knowledge, the observation that *Pa*BqsR binds Fe^{2+} directly represents the first example in which a cytosolic RR of a TCS binds and responds to the same signal/stimulus that is sensed extracytoplasmically by its cognate HK, and these data demonstrate an important functional divergence in this RR compared to other members of the OmpR-like family. When our *in vivo* observations are taken together with the unprecedented finding that *Pa*BqsR binds Fe^{2+} directly, we believe these data point to a dual role for *Pa*BqsR in regulating Fe^{2+} uptake in PAO1 both via the BqsRS sensing axis directly and via the bioavailable pool of Fe^{2+}, independent of BqsS, in order to respond rapidly to changes in Fe^{2+} levels so as to prevent toxic levels of Fe^{2+} from accumulating within the bacterium.

DISCUSSION

TCSs are known to play a key role in the production of virulence factors by infectious bacteria,[5,55] allowing for these pathogens to adapt and to establish infection within diverse environments of host organisms. As just a couple of examples, the *E. coli* PhoPQ TCS alters the ability of *E. coli* to survive when challenged to antibiotics,[56,57] while the *F. tularensis* QseBC TCS alters bacterial motility for downstream infection.[58] Germane to this work, the *P. aeruginosa* BqsRS TCS regulates the production of the virulence factor pyocyanin,[22] the expression of genes involved in biofilm formation,[20] and the expression of genes involved in antibiotic resistance.[21] Despite this critical link between TCS function and the establishment of infection,[20] our understanding of how a membrane HK selects for its cognate stimulus, and how its cognate RR is selective for target genes both remain understudied, particularly for the Fe^{2+}-sensing *Pa*BqsRS system. While *Pa*BqsS was recently characterized at the protein level,[33] its cognate partner, *Pa*BqsR, had not been. Based on sequence homology, *Pa*BqsR was predicted to be an OmpR/PhoB-like RR,[21] the most common family of RR present in Gram-negative bacteria.[59] Consistent with this notion, our X-ray crystal structure of the *Pa*BqsR receiver domain reveals a $(\beta\alpha)_5$ response regulator assembly consisting of a central five-stranded parallel β-sheet surrounded by five α-helices with an overall strong structural homology to members of the OmpR-like family. Stretching to the surface of the domain is the Asp residue (Asp^{51}) conserved across the OmpR-like family that receives the phosphate moiety from the HK to set into motion the downstream DNA-binding process, mediated by the *Pa*BqsR DBD. Our NMR structure reveals that the *Pa*BqsR DBD comprises a trihelical helix-turn-helix (HTH) fold that is common for a number of DNA-binding proteins.[35–39] As the DBDs of RRs determine promoter sequence recognition within an organism,[50] and as our previous work demonstrated that the membrane HK of the BqsRS system, *Pa*BqsS, was

selectively activated by Fe^{2+},[33] we then considered whether *Pa*BqsR might target one or several genes related to Fe^{2+} homeostasis. Indeed, we have now shown that the BqsR box is found in the promoter region of *feo*, and *in vitro* EMSAs with recombinantly-produced, pseudo-activated *Pa*BqsR confirmed its ability to bind to the upstream region of *feo*, which is dependent on a critical β-hairpin residue in the *Pa*BqsR DBD (Arg^{211}) for recognition of the BqsR box, helping define the structural basis of DNA binding by this OmpR-like RR that we then explored *in vivo*.

Consistent with our *in vitro* EMSA results showing *Pa*BqsR binding to the BqsR box upstream of the *feo* operon, we then demonstrated that the *feo* operon is one of the top *Pa*BqsR-regulated pathways *in vivo*. RNA-seq analysis revealed that, during aerobic growth of PAO1 in the presence of 4 μM Fe^{2+}, transcription of the *feo* operon was negatively regulated by *Pa*BqsR. Although *feo* genes have not been reported as a part of the anaerobic BqsSR regulon in response to 200 μM Fe^{2+},[21,31] negative regulation of *feo* by *Pa*BqsR can be concluded from the follow-up study,[60] where 50 μM Fe^{2+} led to increased *bqsR* expression but decreased *feo* expression. To gain further insight into this regulation, we then performed P^{feo}-*lux* reporter assays and observed that the addition of 100 μM Fe^{2+} to aerobically grown PAO1 repressed P^{feo}-*lux* expression during early exponential phase in the WT strain, with significantly stronger repression in Δ*bqsR*. This observation suggests that *Pa*BqsR acts as a positive regulator of *feo* under these conditions, potentially in coordination with the global regulator FUR.[61] Despite differences in P^{feo}-*lux* expression, no significant growth differences were observed during this phase. However, during the transition to stationary phase, P^{feo}-*lux* expression was higher in the Δ*bqsR* mutant compared to the WT strain, indicating a switch to negative regulation by *Pa*BqsR. This regulatory shift coincided with a pronounced growth defect in the Δ*bqsR* strain after exposure to 100 μM Fe^{2+}, but not after exposure to 4 μM Fe^{2+}, likely due to iron toxicity from unfettered Fe^{2+} accumulation.

These exciting findings suggest that *Pa*BqsR operates in two modes to control *feo* regulation, positive and negative, with a switch occurring during the progression to stationary phase and increasing at higher Fe^{2+} concentrations, which may be linked to the ability of *Pa*BqsR to bind Fe^{2+} directly, shown here for the first time and unprecedented among OmpR-like RRs to our knowledge. It is noteworthy that *Pa*BqsR-dependent regulation was detected at 4 μM Fe^{2+}, in contrast to the previously reported 10 μM Fe^{2+} required for *Pa*BqsR expression,[31] which may reflect differences in strain background (PAO1 *vs*. PA14) or growth conditions (aerobic vs anaerobic). Furthermore, elevated *feo* transcript levels have been detected in CF sputum compared to *in vitro* conditions,[60,62,63] suggesting the importance of Fe^{2+} homeostasis for *P. aeruginosa* survival during infection. This assertion is substantiated by the evidence that Fe^{2+} abundance increases with the progression of CF lung infections, becoming the dominant iron source,[60] thereby necessitating tight regulation of the Feo system to balance iron acquisition without causing toxicity. Our study is the first to detail this *Pa*BqsR-dependent mechanism controlling the regulation of *feo* and its biological significance, highlighting *Pa*BqsR as a key component in the intricate regulatory network governing iron homeostasis in *P. aeruginosa* (Fig. 7).

While previous studies have shown that *Pa*BqsR regulates gene expression during aerobic[22] and anaerobic[21,31] growth of *P. aeruginosa* strains, the scope of this important protein's regulatory impact on the global PAO1 gene landscape had not been defined. In this work, we identified a large regulon comprising *ca*. 43% of the PAO1 genome (≥ 2 LFC), 37 % of which belongs to moderate and top responders (≥ 3 LFC), expanding the repertoire of *Pa*BqsR-regulated genes to include iron uptake, urea metabolism, vitamin B_{12} synthesis, lipopolysaccharide (LPS) synthesis/modification, and even phosphate and sulfur uptake. The previously reported *Pa*BqsR regulon in response to Fe^{2+} shock in PA14 was relatively small, including only 46 induced

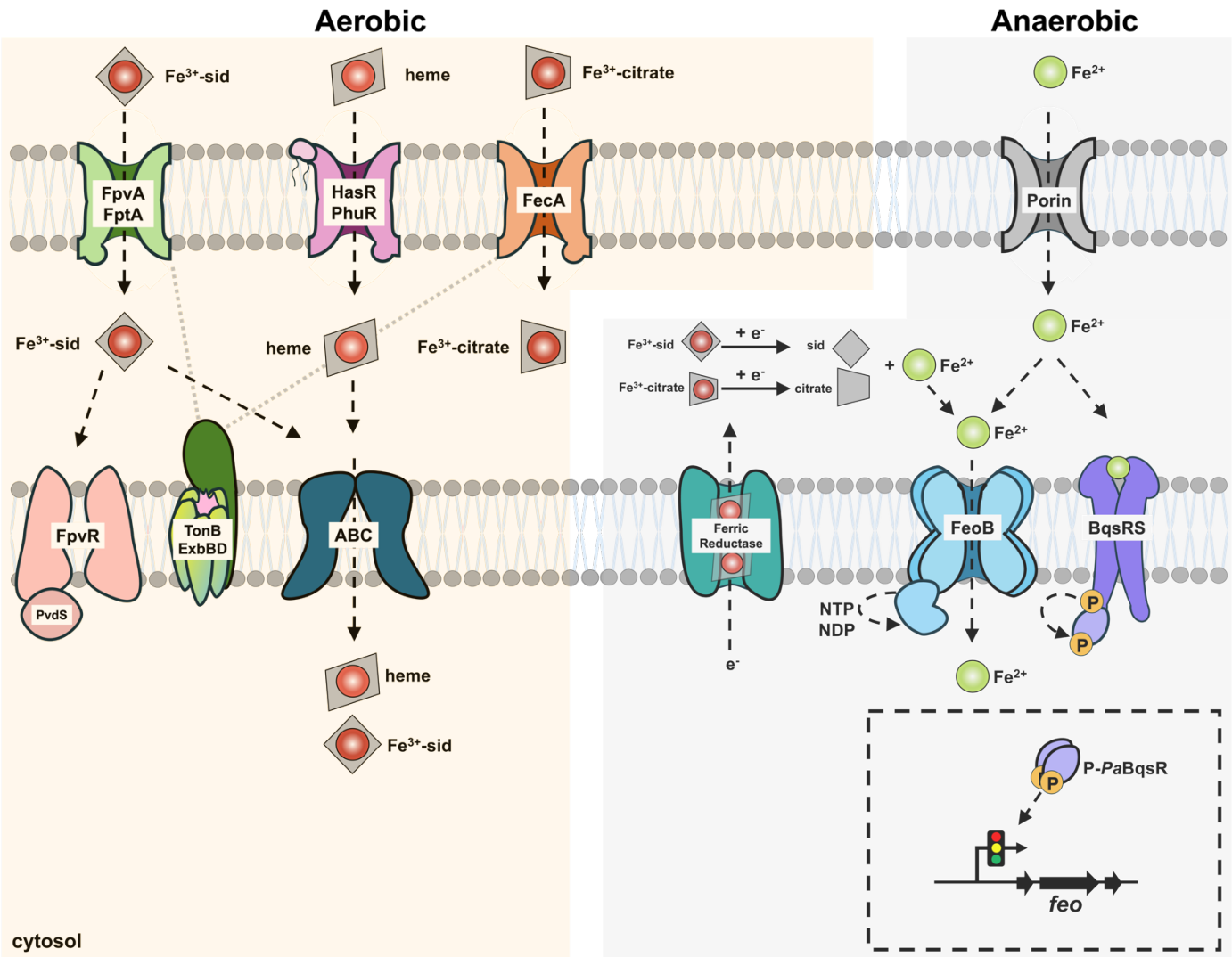

Figure 7. Cartoon of the primary iron homeostasis pathways in *P. aeruginosa* and their relationships to BqsRS. Under oxic conditions, chelated Fe^{3+}-siderophore complexes such as pyoverdine are shuttled into the periplasm by outer membrane proteins such as FpvA and FptA. Fe^{3+}-citrate uptake is accomplished by FecA. Iron protoporphyrin IX (heme *b*) is sensed and imported by the HasR/PhuR system. These chelated iron complexes are typically brought into the cytosol via ABC transporters, although other mechanism may strip the chelates of the iron itself. Under anoxic conditions, Fe^{2+} is thought to diffuse into the periplasm through outer membrane porins or may be generated in the periplasmic space by ferric reductases. The Feo system then transports Fe^{2+} into the cytosol. The Fe^{2+}-specific TCS BqsRS directly senses Fe^{2+} and dynamically regulates *feo* (among other genes), which is shown here for the first time.

genes,[21,31]k nine of which were also induced during growth at 4 μM Fe^{2+} (such as *carO* and *carP* that play a role in oxidative stress tolerance and pyocyanin production).[22,64] Furthermore, the Fe^{2+}-shocked *Pa*BqsR regulon included 14 genes that were induced under high-iron conditions but, according to our RNA-seq data, are repressed by *Pa*BqsR during growth at 4 μM Fe^{2+}, further underscoring that *Pa*BqsR regulation switches from activation to repression depending on iron

concentrations. Interestingly, in response to Fe^{2+} shock, *Pa*BqsR induced the expression of the *pmrAB* TCS that controls lipopolysaccharide modification genes but was thought to be only Fe^{3+}-responsive.[65] In contrast, here we show that *Pa*BqsR represses *pmrAB* and lipopolysaccharide modification genes during growth at 4 μM Fe^{2+}. These findings reveal that different environmental cation concentrations modulate *Pa*BqsR regulation of target genes, indicating its capacity to function as a dynamic global regulator. A similar phenomenon has been described for the HK GacS in *P. aeruginosa*, where three different sensor kinases can phosphorylate GacS in response to different stimuli.[66] Considering the physiological significance of the pathways regulated by *Pa*BqsR, this regulatory flexibility likely enhances the ability of *P. aeruginosa* to adapt and to survive within diverse environments and host-associated niches in which nutrients, such as Fe^{2+}, may be withheld and dramatically change in their availability. Given this importance, the BqsRS system may represent a very attractive future therapeutic target to treat *P. aeruginosa* infections.

Acknowledgements

This work was supported by NIH-NIGMS grant R35 GM133497 (A.T.S), NIH-NIGMS grant T32 GM158458 (A. T. S. and A. P.), HHMI Gilliam Fellowship GT15765 (A. P.), NIH-NIGMS grant R15 GM124670 (M.A.P.), grant CFF-005124P222 (M.A.P.), and the Murdock Trust Swanson Promise for Scientific Research Award (K.N.C.). Use of the Stanford Synchrotron Radiation Lightsource, SLAC National Accelerator Laboratory, is supported by the U.S. Department of Energy, Office of Science, Office of Basic Energy Sciences under Contract No. DE-AC02-76SF00515. The SSRL Structural Molecular Biology Program is supported by the DOE Office of Biological and Environmental Research, and by the National Institutes of Health, National Institute of General Medical Sciences (P30GM133894). The contents of this publication are solely the responsibility of the authors and do not necessarily represent the official views of NIGMS or NIH. Sequence searches utilized both database and analysis functions of the Universal Protein Resource (UniProt) Knowledgebase and Reference Clusters (http://www.uniprot.org) and the National Center for Biotechnology Information (http://www.ncbi.nlm.nih.gov/). We thank Dr. Chelsea Murphy at the Oklahoma State University Bioinformatic Center for her assistance with RNA-seq plots. We also thank Jacob Burch-Konda for the initial analysis of the RNA sequencing data.

Author contributions

A.P., M.H., H.S., J.B.B., K.N.C., M.A.P., and A.T.S. designed the research; A.P., M.H., H.S., D.G., A.J.N., A.K.; J.B.B., and K.N.C. performed the research; A.P, M.H., H.S., K.N.C., M.A.P., and A.T.S. analyzed the data; A.P., M.H., H.S., K.N.C., M.A.P., and A.T.S. wrote and edited the paper.

Additional information

Supplementary information. Supplementary information accompanies this paper that includes supplementary figures S1-S10, supplementary tables S1-S6, as well as any additional experimental details, materials, and methods.

Competing interests

The authors declare no competing interests.

METHODS

Materials. All codon-optimized genes used in this study were synthesized and verified by GenScript. Materials used for buffer preparation, protein expression, and protein purification were purchased from standard commercial suppliers and were used as received. Isotopically-enriched ammonium chloride ($^{15}NH_4Cl$) and glucose (globally $^{13}C_6$-labeled) were purchased from Cambridge Isotope Laboratories and used as received. All DNA primers and duplexes used for EMSAs were synthesized and verified by Integrated DNA Technologies. D_2O was purchased from MilliporeSigma and used as received.

Bacterial strains and media. Strains and plasmids used in this study are listed in Table S6. *P. aeruginosa* strain PAO1 is the most commonly used non-mucoid strain originally isolated from a wound infection that was sequenced first[67] and become a reference strain for *Pseudomonas* genetics and functional studies.[68] All the strains in this study were maintained in 10 % skim milk at −80 °C. For each experiment, bacteria were inoculated from frozen stocks onto LB agar containing the appropriate antibiotic when applicable and grown overnight at 37 °C, from which isolated colonies were used to inoculate precultures. PAO1 and its derivatives were grown in the biofilm minimal medium (BMM)[69] that was modified and designated BMM8.5 with the following composition: 9.0 mM sodium glutamate, 5 mM glycerol, 0.08 mM $MgSO_4$, 0.15 mM NaH_2PO_4, 0.34 mM K_2HPO_4, 145 mM NaCl, 200 µL trace metals, and 1 mL vitamin solution (per L of medium). The trace-metals solution was prepared with 5.0 g $CuSO_4 \cdot 5H_2O$, 5.0 g $ZnSO_4 \cdot 7H_2O$, and 2.0 g $MnCl_2 \cdot 4H_2O$ per liter of 0.83 M hydrochloric acid. The vitamin solution was prepared by dissolving 0.5 g thiamine and 1 mg biotin (per L of the final medium). Filter sterilized trace metals, $MgSO_4$, and the vitamin solution were added aseptically to autoclaved media and adjusted

to a pH of 7.0. This prepared BMM8.5 contains no iron and was designated no-iron-BMM8.5. To prepare BMM8.5 with added iron, $FeSO_4$ was prepared as 100x stocks containing either 360 μM or 10 mM iron. To minimize the oxidation of Fe^{2+}, 100 mM ascorbic acid was dissolved in the water prior to mixing in $FeSO_4$ (1 mM final). The stocks were then filter sterilized and added to the no-iron-BMM8.5 to a final concentration of 4 μM or 100 μM of $FeSO_4$.

Protein expression and purification. Codon-optimized DNA blocks encoding for *Pseudomonas aeruginosa* strain PAO1 BqsR (Uniprot identifier Q9I0I1) with either intact (amino acids 1-223, WT *Pa*BqsR) or the C-terminal DNA-binding domain (amino acids 123-223, *Pa*BqsR DBD) modified to encode for an additional C-terminal tobacco etch virus (TEV) protease site (ENLYFQS) were commercially synthesized by Genscript. These DNA sequences were then subcloned into the pET-21a(+) expression vector such that the resulting expression construct was read in-frame with a terminating C-terminal $(His)_6$ tag. Generation of the intact D51E variant of *Pa*BqsR was accomplished using site-directed mutagenesis. Mutations to the WT *Pa*BqsR expression plasmid was accomplished by the QuikChange Lightning Multi Site-Directed Mutagenesis kit (Agilent). The following primers were used to introduce the mutated bases (underlined): (D51E forward: 5'-CCCGGCAGACCCAGTTCCAGAATGATCAG-3'; D51E reverse: 5'-CTGATCATTCTGGAACTGGGTCTGCCGGG-3'; R211A forward: 5'-CGAAACCCGTGCTGGTCAAGGTTAC-3'; R211A reverse: 5'-GTAACCTTGACCAGCACGGGTTTCG-3'; R211K forward: 5'-CGAAACCCGTAAAGGTCAAGGTTAC-3'; R211K reverse: 5'-GTAACCTTGACCTTTACGGGTTTCG-3'). The presence of the appropriate mutation was verified by nanopore DNA sequencing. Each expression plasmid was electroporated into

electrocompetent *Escherichia coli* BL21 (DE3) cells, spread onto Luria Broth (LB) agar plates supplemented with 0.1 mg/mL ampicillin (final), and grown overnight at 37 °C. Large-scale expression of all natural-abundance *Pa*BqsR constructs (intact WT, D51E, R211A, R211K, D51E/R211A, D51E/211K, or the DBD) in rich media was accomplished in 6 baffled flasks each containing 1 L sterile LB supplemented with 0.1 mg/mL ampicillin (final) and inoculated with a pre-culture derived from a single bacterial colony. Cells were shaken at 200 RPM until the optical density (OD) at 600 nm (OD_{600}) reached *ca*. 0.6-0.8. Cell cultures were then cold-shocked for approximately 2 hours at 4 ºC before being induced with 1 mM (final) isopropyl β-D-1-thiogalactopyranoside (IPTG) and incubated at 18 ºC overnight with continued shaking. Cells were then harvested by centrifugation for 12 min at 5000×*g* and 4 ºC and resuspended with a cellular resuspension buffer (50 mM Tris, pH 7.5, 300 mM NaCl, 10 % (v/v) glycerol, 1 mM TCEP). Immediately prior to cell lysis, solid phenylmethylsulfonyl fluoride (PMSF, *ca.* 50-100 mg) was added to the cellular suspension. Cells were then kept cold in an ice bath while being disrupted via sonication (80 % maximal amplitude, 30 s on pulse, 30 s off pulse, 12 min total time on). The resulting lysate was clarified by ultracentrifugation at 160,000×*g*, 4 ºC for 1 hr. The clarified lysate was then purified via immobilized metal affinity chromatography (IMAC) and size-exclusion chromatography (SEC). Briefly, the lysate was injected onto a prepacked 5 mL HisTrap HP column (Cytiva). The column was then washed with 5 column volumes (CVs) of wash buffer (50 mM Tris, pH 7.5, 300 mM NaCl, 10 % (v/v) glycerol, 1 mM TCEP) and eluted stepwise with 7.0 %, 16.7 %, 50.0 %, and 100.0 % (all v/v) respective concentrations of elution buffer (the same composition of the wash buffer plus 300 mM imidazole). Fractions containing *Pa*BqsR were pooled and concentrated using a 10 kDa molecular weight cutoff (MWCO) Amicon spin concentrator. The protein was then buffer exchanged into a TEV cleavage buffer (50 mM Tris, pH

8.0, 200 mM NaCl, 5 % (v/v) glycerol, 1 mM TCEP, 0.5 mM EDTA) by repeated concentration and dilution in the same spin concentrator. A mixture was then made comprising *ca*. 20 µg TEV protease per *ca*. 1 mg protein and allowed to rock at 4 ºC overnight. Following tag cleavage, the protein sample was applied to a HiLoad 10/300 GL Superdex 75 preparative SEC column (Cytiva) pre-equilibrated with SEC buffer (50 mM Tris, pH 7.5, 100 mM NaCl, 5 % (v/v) glycerol, 1 mM TCEP) and eluted isocratically. Fractions containing monomeric protein were collected, quantified, and analyzed using 15 % SDS-PAGE and Western blotting. The phosphomimetic *Pa*BqsR-BeF_3^- complex was generated by incubating WT *Pa*BqsR with 7 mM $MgCl_2$, 5.3 mM $BeSO_4$, and 35 mM NaF (all final concentrations) prior to further experimentation.

Crystallization and data collection. Initial crystals of *Pa*BqsR were obtained using sparse-matrix screening applying the sitting-drop vapor-diffusion method. Crystals were subsequently optimized by sitting-drop vapor-diffusion using MiTeGen-XtalQuest Plates with a 1:1 (v:v) of *Pa*BqsR (*ca.* 10 mg/mL) and reservoir solution mixture at room temperature. The precipitant solution consisted of 1.0 M sodium/potassium phosphate at pH 8.2. Medium, three-dimensional, colorless octahedral crystals appeared within 72 hr and reached their maximal sized within 7 days (on average). Crystals were transferred into cryoprotectant, looped, flash-frozen, and stored in liquid N_2. Data sets were collected on beamlines LS-CAT 21-ID-F at the Advanced Photon Source, Argonne National Laboratory, using a Marmosaic 300 mm CCD detector. Data were processed automatically with Xia2.[70] Phases were determined via molecular replacement using Phaser in Phenix[71] with an input of a truncated *Pa*BqsR AlphaFold model (AF-Q9I0I1-F1-v4). Extended model building and refinement cycles were performed in Coot[72] and Phenix Refine[71] respectively, and final validations were performed using Phenix Validate.[71] The final model consists of the N-terminal receiver

domain of *Pa*BqsR (amino acids 1-123) and has been deposited in the Protein Data Bank (PDB ID 8GC6).

Nuclear magnetic resonance (NMR) spectroscopy. In order to isotopically-label *Pa*BqsR (intact WT, D51E, or the DBD), the cellular growth and protein production processes were both slightly modified. Briefly, *E. coli* BL21 (DE3) cells containing each expression plasmid grown in minimal media (1x M9 minimal salts, 1 mM $MgSO_4$, 1x trace elements, 0.1 mM $ZnCl_2$, 0.1 mM $CaCl_2$, and 1x MEM vitamin solution) supplemented with $^{15}NH_4Cl$, $^{13}C_6$-glucose, or both, for global nitrogen and carbon labeling, respectively. Cells were then grown with shaking, induced, harvested, resuspended, and lysed in the same manner as cells grown in rich media (*vide supra*). Isotopically-labeled *Pa*BqsR proteins were purified in the same way as their natural-abundance isotopologues (*vide supra*). Once purified, isotopically-labeled *Pa*BqsR proteins (intact WT, D51E, or the DBD) were then buffer exchanged into an NMR-compatible buffer (50 mM sodium phosphate, pH 5.5, 5 mM NaCl, 1 mM DTT, and 10 % (v/v) D_2O). All NMR spectra were acquired at 25 °C on either a Bruker 800 MHz spectrometer or a Bruker 600 MHz spectrometer equipped with a cryogenic probe. Protein backbone resonance assignments of the *Pa*BqsR DBD were achieved by standard triple resonance experiments, including HNCA, HBHA(CO)NH, HNCACB, CBCA(CO)NH, and HNCO.[73–77] Consensus chemical shift index (CSI) (Hα, Cα, and Cβ and C0) of the *Pa*BqsR DBD were calculated using the program CSI 3.0.[78] Both ^{13}C- and ^{15}N-labeled three-dimensional nuclear Overhauser effect spectroscopy (NOESY) data were collected in order to calculate the lowest-energy tertiary fold conformers of the *Pa*BqsR DBD. The solution structure of the *Pa*BqsR DBD was calculated using CYANA 3.98.15.[79] Distance restraints were generated by picking NOE peaks using NMR Analyst[80] followed by automated NOE cross-peak assignment with CYANA

3.98.15.[79,81] Upper interproton distance limits of 2.7 Å, 3.3 Å, and 5.0 Å were used for NOE cross-peaks of strong, medium, and weak intensities, respectively. The TALOS+ Server was used to determine backbone dihedral restraints that were incorporated into structural calculations based on amide proton, amide nitrogen, Hα, Cα, Cβ, and carbonyl carbon chemical shifts.[82] Hydrogen bond restraints were determined based on structure assignments given by the Cα chemical shift indices and strong NOE patterns.[83] A list of restraint statistics is provided in Table S2. UCSF ChimeraX was employed to prepare structural figures.[84] Out of the 160 calculated conformers, the atomic coordinates of the 20 *Pa*BqsR DBD conformers with the lowest target functions were deposited to the PDB (PDB ID 9FYA). NMR chemical shifts and corresponding structure refinement parameters were deposited in the BMRB database (BMRB accession number 31268).

Multiple sequence alignments. Response regulators in which the structures of their DNA-binding domains have been experimentally determined were extracted from the PDB, and their sequences were obtained from the Uniprot database. A multiple sequence alignment was constructed through the EMBL MUSCLE program using default parameters.[85] The resultant alignment was visualized on the MEGAX software.[86]

Electrophoretic mobility shift assays. Electrophoretic mobility shift assays (EMSAs) were performed in order to test the DNA binding capabilities of *Pa*BqsR to the upstream region of the PAO1 *feo* operon. Increasing concentrations of either intact WT, D51E, R211A, R211K, D51E/R211A, D51E/R211K, or BeF_3^--activated *Pa*BqsR were incubated for 30 minutes at room temperature in SEC buffer with a constant concentration of double stranded *feo* DNA containing the BqsR box (5'-CCTTAAGCGAGCCTTAAGTGA-3' and 5'-

TCACTTAAGGCTCGCTTAAGG-3'). Analyses were then performed at 4 °C using a 5 % acrylamide gel (0.5 % TB, 29:1 acrylamide:bis-acrylamide). DNA was stained using ethidium bromide and visualized with an ultraviolet (UV) transilluminator.

Structural modeling. All AlphaFold models were generated from the predicted AlphaFold Protein Structure Database[87] or modeled *de novo* using the AlphaFold3 structure prediction server.[88] To generate the intact WT and D51E *Pa*BqsR models bound to the PAO1 *feo* uptstream region, two copies of the respective protein sequences were used as input into the AlphaFold3 structure prediction server along with the following DNA duplex sequence: 5'-TCCACTCCGATACTGCGTCCTTAAGCGAGCCTTAAGTGAGAGTCGTTTAGATTCTC-3' and 5'-GAGAATCTAAACGACTCTCACTTAAGGCTCGCTTAAGGACGCAGTATCGGAGTGGA-3'. AlphaFold3 structural predictions were carried out without any modifications of the input parameters.

Growth studies. *P. aeruginosa* strains were grown in no iron-BMM8.5 at 37 °C until mid-log phase (12 h), after which they were normalized to an OD_{600} of 0.3 and inoculated 1:100 into fresh medium (BMM8.5) containing 4 μM or 100 μM $FeSO_4$ and 1 mM ascorbic acid. Cultures were grown statically (to minimize oxidation of Fe^{2+}) in clear 96-well plates at 37 °C for 36 h in a BioTek SynergyMx. The absorbance at 600 nm was measured hourly. Every experiment contained at least three independent biological replicates and was repeated at least twice for consistency.

RNA sequencing. Total RNA was collected from mid-log phase WT PAO1 and Δ*bqsR* cells grown in BMM using the RNeasy Mini Kit (Qiagen). Purified RNA was treated with Turbo DNase (Invitrogen) and contaminating DNA was assessed using PCR with primers specific for the 16S rRNA gene (forward 5'-GTGCCAGCAGCCGCGGTAA-3'; reverse 5'-AGGGTTGCGCTCGTTG-3'). RNA concentrations were determined using a NanoDrop spectrophotometer (Thermo Scientific) and the RNA quality was analyzed using an RNA 6000 Nano Chip on a Bioanalyzer 2100 (Agilent) and by 1.2 % agarose gel electrophoresis. RNA samples with A_{260}/A_{280} ratio of 1.8-2.0 and an RIN value ≥ 7.0 were selected for sequencing analysis. Ribosomal RNA was removed using the Ribo-Zero rRNA Depletion Kit (Illumina). For sequencing, 250-300 bp insert size, strand-specific libraries were prepared and sequenced by Novogene Co., Ltd using paired-end sequencing (2 x 150 bp) on a Nova Seq 6000 platform.

Analysis of RNA-seq reads. All raw RNA sequences were further analyzed using Kbase (https://www.kbase.us/). Three biological replicates were used for each stain. Reads were checked for quality using FastQC-v0.11.5 and trimmed using Trimmomatic-v0.36. The trimmed reads were aligned to the PAO1 genome using HISAT2-v2.1.0 and assembled using Cufflinks-v2.2.1. A differential expression matrix was generated using DESeq2-v1.20.0, and the resulting raw gene count matrix was uploaded to iDEP2.01 (http://bioinformatics.sdstate.edu/idep/) to determine $\log_2$ of fold change (FC) in gene expression in Δ*bqsR* compared to WT along with their false discovery rate (adjusted *p*-values). A volcano plot depicting differentially expressed genes ($\log_2 FC > |1|$) with significant -log10 *p*-values (> 1.3 for $p < 0.05$) was generated using Rstudio. The differentially expressed genes were sorted into functional categories using annotations from Gene Ontology (https://www.geneontology.org/), Kyoto Encyclopedia of Genes and Genomes (KEGG)

(https://www.kegg.jp/kegg/pathway.html), and the Pseudomonas Community Annotation Project (PseudoCAP) (https://pseudomonas.com/). Heatmaps of selected pathways were generated using MORPHEUS (https://software.broadinstitute.org/morpheus/).

Construction of the *feo* promoter (P^{feo}) fusion reporter. A 300 bp region upstream of the *feo* operon was amplified from the PAO1 genome using the primers: XhoI_feo_pro_F and BamHI_feo_pro_R (Table S6). Following column purification, the purified PCR product and the pCTX-1-*lux* vector were digested using the restriction enzymes XhoI and BamHI. The digested insert was ligated into pCTX-1-*lux* directly upstream of the *luxCDABE* operon. The ligated product was transformed into heat-shock competent *E. coli* DH5α cells. Successful transformants were selected on LB agar plates containing 10 µg/mL tetracycline (Tet^{10}). The resultant constructs were verified to have the insert by Nanopore DNA sequencing performed by Plasmidsaraus and are hereafter referred to as pKen04. The pKen04 promoter construct was heat-shock transformed into the *E. coli* SM10 mating strain. Transformants were selected on Tet^{10} LB agar plates. The SM10 strain harboring the pKen04 construct was further conjugated with relevant *P. aeruginosa* strains by biparental mating.[90] Successful transconjugants were selected on LB agar supplemented with 60 µg/mL Tet (Tet^{60}), replica plated on Tet^{60} plates, and PCR-verified using *bqsR* specific primers XbaI_bqsR_F and XhoI_bqsR_R (Table S6).

Promoter assays. *P. aeruginosa* strains were grown in BMM8.5 containing 4 µM $FeSO_4$ at 37 °C until mid-log phase (12 h), normalized to an OD_{600} of 0.3, and inoculated 1:100 into fresh BMM8.5 containing 4 µM $FeSO_4$. Cultures were incubated statically at 37 °C in white 96-well plates. After six hours, the cultures were treated with $FeSO_4$ solutions prepared in ascorbic acid to achieve a

final concentration of 4 μM or 100 μM $FeSO_4$ and 1 mM ascorbic acid. Treated cultures were then continuously incubated statically at 37 °C, and luminescence and absorbance readings at 600 nm were measured immediately after treatment and subsequently at hourly intervals. Relative luminescence units (RLU) were calculated by normalizing by OD_{600}. Every experiment contained at least three independent biological replicates and was repeated at least twice for consistency.

Metal-binding assays. $(His)_6$-cleaved *Pa*BqsR constructs (intact WT, D51E, or DBD) were tested for their ability to bind Fe^{2+}. Briefly, each construct was degassed and brought into an anoxic chamber containing an N_2/H_2 atmosphere and operating at < 5 ppm O_2. After overnight equilibration with the N_2/H_2 atmosphere, each protein solution was incubated with 1-5 mol eq. of Fe^{2+} to assess stability of the protein in the presence of metal. The intact protein only tolerated a maximal loading of 1.2 mol eq. of Fe^{2+}, so all metal-loading experiments were performed with this slight excess of metal cation in solution. After the addition of metal and incubation for 10 min at *ca.* 6 °C, the protein-metal solution was buffer exchanged into SEC buffer (50 mM Tris, pH 7.5, 100 mM NaCl, 5 % (v/v) glycerol, 1 mM TCEP) through extensive rounds of concentration and dilution using a 0.5 mL 10 kDa MWCO spin concentrator. A modified version of the ferrozine assay[91,92] was performed as previously described.[93] All metal loading was then further confirmed by measuring metal content using a PerkinElmer NexION 300D mass spectrometer connected to inductively couple plasmon mass spectrometry (ICP-MS).

X-ray absorption spectroscopy (XAS). Intact WT *Pa*BqsR samples were metal-loaded anoxically and concentrated to *ca.* 2 mM Fe^{2+} (final concentration), mixed anoxically with ethylene glycol (20% (v/v) final), and were aliquoted anoxically into Lucite cells wrapped with

Mylar tape, flash-frozen in liquid N_2 and stored at -80 ºC until data collection. X-ray absorption spectroscopy (XAS) was performed on beamlines 7-3 and 9-3 at the Stanford Synchrotron Radiation Lightsource (Menlo Park, CA), and samples in replicates were collected when possible. Extended X-ray absorption fine structure (EXAFS) of Fe (7210 eV) was measured using a Si 220 monochromator with crystal orientation φ = 90°. Samples were measured as frozen aqueous glasses at 15 K, and the X-ray absorbance was detected as Kα fluorescence using either a 100-element (beamline 9-3) or 30-element (beamline 7-3) Ge array detector. A Z-1 metal oxide filter (Mn) and slit assembly were placed in front of the detector to attenuate the elastic scatter peak. A sample-appropriate number of scans of a buffer blank were measured at the absorption edge and subtracted from the raw data to produce a flat pre-edge and eliminate residual Mn Kβ fluorescence of the metal oxide filter. Energy calibration was achieved by placing a Fe metal foil between the second and third ionization chamber. Data reduction and background subtraction were performed using EXAFSPAK (Microsoft Windows version).[94] The data from each detector channel were inspected for drop outs and glitches before being included into the final average. EXAFS simulation was carried out using the program EXCURVE (version 9.2) as previously described.[94–96] The quality of the fits was determined using the least-squares fitting parameter, *F*, which referred to as the fit index (FI) and is defined as:

$$F^2 = \frac{1}{N}\sum_{i=0}^{N} k^6(\chi_i^{theory} - \chi_i^{exp})^2 \qquad (1)$$

References

(1) Parkinson, J. S.; Kofoid, E. C. COMMUNICATION MODULES IN BACTERIAL SIGNALING PROTEINS. *Annu. Rev. Genet.* **1992**, *26* (Volume 26, 1992), 71–112. https://doi.org/10.1146/annurev.ge.26.120192.000443.

(2) Gupta, A.; Gupta, R.; Singh, R. L. Microbes and Environment. *Princ. Appl. Environ. Biotechnol. Sustain. Future* **2016**, 43–84. https://doi.org/10.1007/978-981-10-1866-4_3.

(3) Chang, C.; Stewart, R. C. The Two-Component System1: Regulation of Diverse Signaling Pathways in Prokaryotes and Eukaryotes. *Plant Physiol.* **1998**, *117* (3), 723–731. https://doi.org/10.1104/pp.117.3.723.

(4) Nixon, B. T.; Ronson, C. W.; Ausubel, F. M. Two-Component Regulatory Systems Responsive to Environmental Stimuli Share Strongly Conserved Domains with the Nitrogen Assimilation Regulatory Genes ntrB and ntrC. *Proc. Natl. Acad. Sci.* **1986**, *83* (20), 7850–7854. https://doi.org/10.1073/pnas.83.20.7850.

(5) Paredes, A.; Iheacho, C.; Smith, A. T. Metal Messengers: Communication in the Bacterial World through Transition-Metal-Sensing Two-Component Systems. *Biochemistry* **2023**, *62* (16), 2339–2357. https://doi.org/10.1021/acs.biochem.3c00296.

(6) Mitrophanov, A. Y.; Groisman, E. A. Signal Integration in Bacterial Two-Component Regulatory Systems. *Genes Dev.* **2008**, *22* (19), 2601–2611. https://doi.org/10.1101/gad.1700308.

(7) Stock, A. M.; Robinson, V. L.; Goudreau, P. N. Two-Component Signal Transduction. *Annu. Rev. Biochem.* **2000**, *69* (Volume 69, 2000), 183–215. https://doi.org/10.1146/annurev.biochem.69.1.183.

(8) Cheng, A. T.; Ottemann, K. M.; Yildiz, F. H. Vibrio Cholerae Response Regulator VxrB Controls Colonization and Regulates the Type VI Secretion System. *PLoS Pathog.* **2015**, *11* (5), e1004933. https://doi.org/10.1371/journal.ppat.1004933.

(9) Chatfield, S. N.; Dorman, C. J.; Hayward, C.; Dougan, G. Role of ompR-Dependent Genes in Salmonella Typhimurium Virulence: Mutants Deficient in Both ompC and ompF Are Attenuated in Vivo. *Infect. Immun.* **1991**, *59* (1), 449–452. https://doi.org/10.1128/iai.59.1.449-452.1991.

(10) Ogura, M.; Yamaguchi, H.; Yoshida Ki, null; Fujita, Y.; Tanaka, T. DNA Microarray Analysis of Bacillus Subtilis DegU, ComA and PhoP Regulons: An Approach to Comprehensive Analysis of B.Subtilis Two-Component Regulatory Systems. *Nucleic Acids Res.* **2001**, *29* (18), 3804–3813. https://doi.org/10.1093/nar/29.18.3804.

(11) Prágai, Z.; Harwood, C. R. Regulatory Interactions between the Pho and Sigma(B)-Dependent General Stress Regulons of Bacillus Subtilis. *Microbiol. Read. Engl.* **2002**, *148* (Pt 5), 1593–1602. https://doi.org/10.1099/00221287-148-5-1593.

(12) Kerr, K. G.; Snelling, A. M. Pseudomonas Aeruginosa: A Formidable and Ever-Present Adversary. *J. Hosp. Infect.* **2009**, *73* (4), 338–344. https://doi.org/10.1016/j.jhin.2009.04.020.

(13) Zhao, A.; Sun, J.; Liu, Y. Understanding Bacterial Biofilms: From Definition to Treatment Strategies. *Front. Cell. Infect. Microbiol.* **2023**, *13*, 1137947. https://doi.org/10.3389/fcimb.2023.1137947.

(14) Chiba, A.; Seki, M.; Suzuki, Y.; Kinjo, Y.; Mizunoe, Y.; Sugimoto, S. Staphylococcus Aureus Utilizes Environmental RNA as a Building Material in Specific Polysaccharide-

Dependent Biofilms. *NPJ Biofilms Microbiomes* **2022**, *8*, 17. https://doi.org/10.1038/s41522-022-00278-z.
(15) Schilcher, K.; Horswill, A. R. Staphylococcal Biofilm Development: Structure, Regulation, and Treatment Strategies. *Microbiol. Mol. Biol. Rev.* **2020**, *84* (3), 10.1128/mmbr.00026-19. https://doi.org/10.1128/mmbr.00026-19.
(16) Mikkelsen, H.; Sivaneson, M.; Filloux, A. Key Two-Component Regulatory Systems That Control Biofilm Formation in Pseudomonas Aeruginosa. *Environ. Microbiol.* **2011**, *13* (7), 1666–1681. https://doi.org/10.1111/j.1462-2920.2011.02495.x.
(17) Wang, D.; Wang, L.; Liu, Q.; Zhao, Y. Virulence Factors in Biofilm Formation and Therapeutic Strategies for *Staphylococcus Aureus*: A Review. *Anim. Zoonoses* **2024**. https://doi.org/10.1016/j.azn.2024.11.003.
(18) Li, Y.-H.; Lau, P. C. Y.; Tang, N.; Svensäter, G.; Ellen, R. P.; Cvitkovitch, D. G. Novel Two-Component Regulatory System Involved in Biofilm Formation and Acid Resistance in Streptococcus Mutans. *J. Bacteriol.* **2002**, *184* (22), 6333–6342. https://doi.org/10.1128/JB.184.22.6333-6342.2002.
(19) Sultan, M.; Arya, R.; Kim, K. K. Roles of Two-Component Systems in Pseudomonas Aeruginosa Virulence. *Int. J. Mol. Sci.* **2021**, *22* (22), 12152. https://doi.org/10.3390/ijms222212152.
(20) Dong, Y.-H.; Zhang, X.-F.; An, S.-W.; Xu, J.-L.; Zhang, L.-H. A Novel Two-Component System BqsS-BqsR Modulates Quorum Sensing-Dependent Biofilm Decay in Pseudomonas Aeruginosa. *Commun. Integr. Biol.* **2008**, *1* (1), 88–96.
(21) Kreamer, N. N.; Costa, F.; Newman, D. K. The Ferrous Iron-Responsive BqsRS Two-Component System Activates Genes That Promote Cationic Stress Tolerance. *mBio* **2015**, *6* (2), e02549-14. https://doi.org/10.1128/mBio.02549-14.
(22) Guragain, M.; King, M. M.; Williamson, K. S.; Pérez-Osorio, A. C.; Akiyama, T.; Khanam, S.; Patrauchan, M. A.; Franklin, M. J. The Pseudomonas Aeruginosa PAO1 Two-Component Regulator CarSR Regulates Calcium Homeostasis and Calcium-Induced Virulence Factor Production through Its Regulatory Targets CarO and CarP. *J. Bacteriol.* **2016**, *198* (6), 951–963. https://doi.org/10.1128/jb.00963-15.
(23) Halmerbauer, G.; Arri, S.; Schierl, M.; Strauch, E.; Koller, D. Y. The Relationship of Eosinophil Granule Proteins to Ions in the Sputum of Patients with Cystic Fibrosis. *Clin. Exp. Allergy J. Br. Soc. Allergy Clin. Immunol.* **2000**, *30* (12), 1771–1776. https://doi.org/10.1046/j.1365-2222.2000.00988.x.
(24) Blomfield, J.; Warton, K. L.; Brown, J. M. Flow Rate and Inorganic Components of Submandibular Saliva in Cystic Fibrosis. *Arch. Dis. Child.* **1973**, *48* (4), 267–274.
(25) Stites, S. W.; Walters, B.; O'Brien-Ladner, A. R.; Bailey, K.; Wesselius, L. J. Increased Iron and Ferritin Content of Sputum From Patients With Cystic Fibrosis or Chronic Bronchitis. *Chest* **1998**, *114* (3), 814–819. https://doi.org/10.1378/chest.114.3.814.
(26) Hazlett, H. F.; Hampton, T. H.; Aridgides, D. S.; Armstrong, D. A.; Dessaint, J. A.; Mellinger, D. L.; Nymon, A. B.; Ashare, A. Altered Iron Metabolism in Cystic Fibrosis Macrophages: The Impact of CFTR Modulators and Implications for Pseudomonas Aeruginosa Survival. *Sci. Rep.* **2020**, *10* (1), 10935. https://doi.org/10.1038/s41598-020-67729-5.
(27) Ghio, A. J.; Roggli, V. L.; Soukup, J. M.; Richards, J. H.; Randell, S. H.; Muhlebach, M. S. Iron Accumulates in the Lavage and Explanted Lungs of Cystic Fibrosis Patients. *J. Cyst. Fibros.* **2013**, *12* (4), 390–398. https://doi.org/10.1016/j.jcf.2012.10.010.

(28) Reid, D. W.; Carroll, V.; O'May, C.; Champion, A.; Kirov, S. M. Increased Airway Iron as a Potential Factor in the Persistence of Pseudomonas Aeruginosa Infection in Cystic Fibrosis. *Eur. Respir. J.* **2007**, *30* (2), 286–292. https://doi.org/10.1183/09031936.00154006.
(29) Donlan, R. M.; Costerton, J. W. Biofilms: Survival Mechanisms of Clinically Relevant Microorganisms. *Clin. Microbiol. Rev.* **2002**, *15* (2), 167–193. https://doi.org/10.1128/cmr.15.2.167-193.2002.
(30) Bailey, T. L.; Boden, M.; Buske, F. A.; Frith, M.; Grant, C. E.; Clementi, L.; Ren, J.; Li, W. W.; Noble, W. S. MEME Suite: Tools for Motif Discovery and Searching. *Nucleic Acids Res.* **2009**, *37* (suppl_2), W202–W208. https://doi.org/10.1093/nar/gkp335.
(31) Kreamer, N. N. K.; Wilks, J. C.; Marlow, J. J.; Coleman, M. L.; Newman, D. K. BqsR/BqsS Constitute a Two-Component System That Senses Extracellular Fe(II) in Pseudomonas Aeruginosa. *J. Bacteriol.* **2012**, *194* (5), 1195–1204. https://doi.org/10.1128/JB.05634-11.
(32) Shah, P.; Swiatlo, E. A Multifaceted Role for Polyamines in Bacterial Pathogens. *Mol. Microbiol.* **2008**, *68* (1), 4–16. https://doi.org/10.1111/j.1365-2958.2008.06126.x.
(33) Paredes, A.; Iheacho, C.; Chacón, K. N.; Smith, A. T. The Pseudomonas Aeruginosa Membrane Histidine Kinase BqsS/CarS Directly Senses Environmental Ferrous Iron (Fe2+). bioRxiv April 6, 2025, p 2025.04.06.647434. https://doi.org/10.1101/2025.04.06.647434.
(34) Frankel, A. D. The Importance of Being Flexible. *Proc. Natl. Acad. Sci.* **1992**, *89* (24), 11653. https://doi.org/10.1073/pnas.89.24.11653.
(35) Blanco, A. G.; Sola, M.; Gomis-Rüth, F. X.; Coll, M. Tandem DNA Recognition by PhoB, a Two-Component Signal Transduction Transcriptional Activator. *Structure* **2002**, *10* (5), 701–713. https://doi.org/10.1016/S0969-2126(02)00761-X.
(36) Martínez-Hackert, E.; Stock, A. M. The DNA-Binding Domain of OmpR: Crystal Structures of a Winged Helix Transcription Factor. *Structure* **1997**, *5* (1), 109–124. https://doi.org/10.1016/S0969-2126(97)00170-6.
(37) Lou, Y.-C.; Wang, I.; Rajasekaran, M.; Kao, Y.-F.; Ho, M.-R.; Hsu, S.-T. D.; Chou, S.-H.; Wu, S.-H.; Chen, C. Solution Structure and Tandem DNA Recognition of the C-Terminal Effector Domain of PmrA from Klebsiella Pneumoniae. *Nucleic Acids Res.* **2014**, *42* (6), 4080–4093. https://doi.org/10.1093/nar/gkt1345.
(38) Narayanan, A.; Paul, L. N.; Tomar, S.; Patil, D. N.; Kumar, P.; Yernool, D. A. Structure-Function Studies of DNA Binding Domain of Response Regulator KdpE Reveals Equal Affinity Interactions at DNA Half-Sites. *PLOS ONE* **2012**, *7* (1), e30102. https://doi.org/10.1371/journal.pone.0030102.
(39) Li, Y.-C.; Chang, C.; Chang, C.-F.; Cheng, Y.-H.; Fang, P.-J.; Yu, T.; Chen, S.-C.; Li, Y.-C.; Hsiao, C.-D.; Huang, T. Structural Dynamics of the Two-Component Response Regulator RstA in Recognition of Promoter DNA Element. *Nucleic Acids Res.* **2014**, *42* (13), 8777–8788. https://doi.org/10.1093/nar/gku572.
(40) Marion, D.; Driscoll, P. C.; Kay, L. E.; Wingfield, P. T.; Bax, A.; Gronenborn, A. M.; Clore, G. M. Overcoming the Overlap Problem in the Assignment of 1H NMR Spectra of Larger Proteins by Use of Three-Dimensional Heteronuclear 1H-15N Hartmann-Hahn-Multiple Quantum Coherence and Nuclear Overhauser-Multiple Quantum Coherence Spectroscopy: Application to Interleukin 1 Beta. *Biochemistry* **1989**, *28* (15), 6150–6156. https://doi.org/10.1021/bi00441a004.

(41) Kay, L. E.; Ikura, M.; Bax, A. Proton-Proton Correlation via Carbon-Carbon Couplings: A Three-Dimensional NMR Approach for the Assignment of Aliphatic Resonances in Proteins Labeled with Carbon-13. *J. Am. Chem. Soc.* **1990**, *112* (2), 888–889. https://doi.org/10.1021/ja00158a070.
(42) Banin, E.; Vasil, M. L.; Greenberg, E. P. Iron and Pseudomonas Aeruginosa Biofilm Formation. *Proc. Natl. Acad. Sci. U. S. A.* **2005**, *102* (31), 11076–11081. https://doi.org/10.1073/pnas.0504266102.
(43) Sánchez-Jiménez, A.; Marcos-Torres, F. J.; Llamas, M. A. Mechanisms of Iron Homeostasis in Pseudomonas Aeruginosa and Emerging Therapeutics Directed to Disrupt This Vital Process. *Microb. Biotechnol.* **2023**, *16* (7), 1475–1491. https://doi.org/10.1111/1751-7915.14241.
(44) Johnson, L.; Mulcahy, H.; Kanevets, U.; Shi, Y.; Lewenza, S. Surface-Localized Spermidine Protects the Pseudomonas Aeruginosa Outer Membrane from Antibiotic Treatment and Oxidative Stress. *J. Bacteriol.* **2012**, *194* (4), 813–826. https://doi.org/10.1128/jb.05230-11.
(45) *Ferric reductase transmembrane component-like domain (IPR013130) - InterPro entry - InterPro*. https://www.ebi.ac.uk/interpro/entry/InterPro/IPR013130/ (accessed 2025-02-02).
(46) Winsor, G. L.; Griffiths, E. J.; Lo, R.; Dhillon, B. K.; Shay, J. A.; Brinkman, F. S. L. Enhanced Annotations and Features for Comparing Thousands of Pseudomonas Genomes in the Pseudomonas Genome Database. *Nucleic Acids Res.* **2016**, *44* (D1), D646–D653. https://doi.org/10.1093/nar/gkv1227.
(47) Sestok, A. E.; Linkous, R. O.; Smith, A. T. Toward a Mechanistic Understanding of Feo-Mediated Ferrous Iron Uptake. *Metallomics* **2018**, *10* (7), 887–898. https://doi.org/10.1039/c8mt00097b.
(48) Kümmerli, R. Iron Acquisition Strategies in Pseudomonads: Mechanisms, Ecology, and Evolution. *BioMetals* **2023**, *36* (4), 777–797. https://doi.org/10.1007/s10534-022-00480-8.
(49) Aggarwal, A. K. Crystallization of DNA Binding Proteins with Oligodeoxynucleotides. *Methods San Diego Calif* **1990**, *1* (1), 83–90. https://doi.org/10.1016/S1046-2023(05)80150-1.
(50) Rhee, J. E.; Sheng, W.; Morgan, L. K.; Nolet, R.; Liao, X.; Kenney, L. J. Amino Acids Important for DNA Recognition by the Response Regulator OmpR *. *J. Biol. Chem.* **2008**, *283* (13), 8664–8677. https://doi.org/10.1074/jbc.M705550200.
(51) Sadotra, S.; Lou, Y.-C.; Tang, H.-C.; Chiu, Y.-C.; Hsu, C.-H.; Chen, C. Structural Basis for Promoter DNA Recognition by the Response Regulator OmpR. *J. Struct. Biol.* **2021**, *213* (1), 107638. https://doi.org/10.1016/j.jsb.2020.107638.
(52) Banse, A. V.; Hobbs, E. C.; Losick, R. Phosphorylation of Spo0A by the Histidine Kinase KinD Requires the Lipoprotein Med in Bacillus Subtilis ▿. *J. Bacteriol.* **2011**, *193* (15), 3949–3955. https://doi.org/10.1128/JB.05199-11.
(53) Dahl, M. K.; Msadek, T.; Kunst, F.; Rapoport, G. The Phosphorylation State of the DegU Response Regulator Acts as a Molecular Switch Allowing Either Degradative Enzyme Synthesis or Expression of Genetic Competence in Bacillus Subtilis. *J. Biol. Chem.* **1992**, *267* (20), 14509–14514. https://doi.org/10.1016/S0021-9258(19)49742-1.
(54) Tierney, A. R.; Rather, P. N. Roles of Two-Component Regulatory Systems in Antibiotic Resistance. *Future Microbiol. 14* (6), 533–552. https://doi.org/10.2217/fmb-2019-0002.

(55) Dziejman, M.; Mekalanos, J. J. Two-Component Signal Transduction and Its Role in the Expression of Bacterial Virulence Factors. In *Two-Component Signal Transduction*; John Wiley & Sons, Ltd, 1995; pp 303–317. https://doi.org/10.1128/9781555818319.ch19.
(56) Groisman, E. A. The Pleiotropic Two-Component Regulatory System PhoP-PhoQ. *J. Bacteriol.* **2001**, *183* (6), 1835–1842. https://doi.org/10.1128/jb.183.6.1835-1842.2001.
(57) Gunn, J. S.; Belden, W. J.; Miller, S. I. Identification of PhoP-PhoQ Activated Genes within a Duplicated Region of the Salmonella Typhimurium Chromosome. *Microb. Pathog.* **1998**, *25* (2), 77–90. https://doi.org/10.1006/mpat.1998.0217.
(58) Bearson, B. L.; Bearson, S. M. D.; Lee, I. S.; Brunelle, B. W. The Salmonella Enterica Serovar Typhimurium QseB Response Regulator Negatively Regulates Bacterial Motility and Swine Colonization in the Absence of the QseC Sensor Kinase. *Microb. Pathog.* **2010**, *48* (6), 214–219. https://doi.org/10.1016/j.micpath.2010.03.005.
(59) Galperin, M. Y. Diversity of Structure and Function of Response Regulator Output Domains. *Curr. Opin. Microbiol.* **2010**, *13* (2), 150–159. https://doi.org/10.1016/j.mib.2010.01.005.
(60) Hunter, R. C.; Asfour, F.; Dingemans, J.; Osuna, B. L.; Samad, T.; Malfroot, A.; Cornelis, P.; Newman, D. K. Ferrous Iron Is a Significant Component of Bioavailable Iron in Cystic Fibrosis Airways. *mBio* **2013**, *4* (4), e00557-13. https://doi.org/10.1128/mBio.00557-13.
(61) Vasil, M. L. How We Learnt about Iron Acquisition in Pseudomonas Aeruginosa: A Series of Very Fortunate Events. *BioMetals* **2007**, *20* (3), 587–601. https://doi.org/10.1007/s10534-006-9067-2.
(62) Cornforth, D. M.; Dees, J. L.; Ibberson, C. B.; Huse, H. K.; Mathiesen, I. H.; Kirketerp-Møller, K.; Wolcott, R. D.; Rumbaugh, K. P.; Bjarnsholt, T.; Whiteley, M. Pseudomonas Aeruginosa Transcriptome during Human Infection. *Proc. Natl. Acad. Sci.* **2018**, *115* (22), E5125–E5134. https://doi.org/10.1073/pnas.1717525115.
(63) Bielecki, P.; Komor, U.; Bielecka, A.; Müsken, M.; Puchałka, J.; Pletz, M. W.; Ballmann, M.; Martins dos Santos, V. A.; Weiss, S.; Häussler, S. Ex Vivo Transcriptional Profiling Reveals a Common Set of Genes Important for the Adaptation of Pseudomonas Aeruginosa to Chronically Infected Host Sites. *Environ. Microbiol.* **2013**, *15* (2), 570–587. https://doi.org/10.1111/1462-2920.12024.
(64) King, M.; Kubo, A.; Kafer, L.; Braga, R.; McLeod, D.; Khanam, S.; Conway, T.; Patrauchan, M. A. Calcium-Regulated Protein CarP Responds to Multiple Host Signals and Mediates Regulation of Pseudomonas Aeruginosa Virulence by Calcium. *Appl. Environ. Microbiol.* **2021**, *87* (10), e00061-21. https://doi.org/10.1128/AEM.00061-21.
(65) Moskowitz, S. M.; Ernst, R. K.; Miller, S. I. PmrAB, a Two-Component Regulatory System of Pseudomonas Aeruginosa That Modulates Resistance to Cationic Antimicrobial Peptides and Addition of Aminoarabinose to Lipid A. *J. Bacteriol.* **2004**, *186* (2), 575–579. https://doi.org/10.1128/jb.186.2.575-579.2004.
(66) Francis, V. I.; Waters, E. M.; Finton-James, S. E.; Gori, A.; Kadioglu, A.; Brown, A. R.; Porter, S. L. Multiple Communication Mechanisms between Sensor Kinases Are Crucial for Virulence in Pseudomonas Aeruginosa. *Nat. Commun.* **2018**, *9* (1), 2219. https://doi.org/10.1038/s41467-018-04640-8.
(67) Stover, C. K.; Pham, X. Q.; Erwin, A. L.; Mizoguchi, S. D.; Warrener, P.; Hickey, M. J.; Brinkman, F. S. L.; Hufnagle, W. O.; Kowalik, D. J.; Lagrou, M.; Garber, R. L.; Goltry, L.; Tolentino, E.; Westbrock-Wadman, S.; Yuan, Y.; Brody, L. L.; Coulter, S. N.; Folger, K. R.; Kas, A.; Larbig, K.; Lim, R.; Smith, K.; Spencer, D.; Wong, G. K.-S.; Wu, Z.; Paulsen,

I. T.; Reizer, J.; Saier, M. H.; Hancock, R. E. W.; Lory, S.; Olson, M. V. Complete Genome Sequence of Pseudomonas Aeruginosa PAO1, an Opportunistic Pathogen. *Nature* **2000**, *406* (6799), 959–964. https://doi.org/10.1038/35023079.
(68) Klockgether, J.; Munder, A.; Neugebauer, J.; Davenport, C. F.; Stanke, F.; Larbig, K. D.; Heeb, S.; Schöck, U.; Pohl, T. M.; Wiehlmann, L.; Tümmler, B. Genome Diversity of Pseudomonas Aeruginosa PAO1 Laboratory Strains. *J. Bacteriol.* **2010**, *192* (4), 1113–1121. https://doi.org/10.1128/jb.01515-09.
(69) Patrauchan, M. A.; Sarkisova, S. A.; Franklin, M. J. Strain-Specific Proteome Responses of Pseudomonas Aeruginosa to Biofilm-Associated Growth and to Calcium. *Microbiol. Read. Engl.* **2007**, *153* (Pt 11), 3838–3851. https://doi.org/10.1099/mic.0.2007/010371-0.
(70) Winter, G. Xia2: An Expert System for Macromolecular Crystallography Data Reduction. *J. Appl. Crystallogr.* **2010**, *43* (1), 186–190. https://doi.org/10.1107/S0021889809045701.
(71) Adams, P. D.; Afonine, P. V.; Bunkóczi, G.; Chen, V. B.; Davis, I. W.; Echols, N.; Headd, J. J.; Hung, L.-W.; Kapral, G. J.; Grosse-Kunstleve, R. W.; McCoy, A. J.; Moriarty, N. W.; Oeffner, R.; Read, R. J.; Richardson, D. C.; Richardson, J. S.; Terwilliger, T. C.; Zwart, P. H. PHENIX: A Comprehensive Python-Based System for Macromolecular Structure Solution. *Acta Crystallogr. D Biol. Crystallogr.* **2010**, *66* (2), 213–221. https://doi.org/10.1107/S0907444909052925.
(72) *(IUCr) Coot: model-building tools for molecular graphics*. https://journals.iucr.org/d/issues/2004/12/01/ba5070/index.html (accessed 2025-02-02).
(73) Sattler, M.; Schleucher, J.; Griesinger, C. Heteronuclear Multidimensional NMR Experiments for the Structure Determination of Proteins in Solution Employing Pulsed Field Gradients. *Prog. Nucl. Magn. Reson. Spectrosc.* **1999**, *34* (2), 93–158. https://doi.org/10.1016/S0079-6565(98)00025-9.
(74) Cavanagh, J. *Protein NMR Spectroscopy: Principles and Practice*; Academic Press, 1996.
(75) Bax, A. Multidimensional Nuclear Magnetic Resonance Methods for Protein Studies. *Curr. Opin. Struct. Biol.* **1994**, *4* (5), 738–744. https://doi.org/10.1016/S0959-440X(94)90173-2.
(76) Kanelis, V.; Forman-Kay, J. D.; Kay, L. E. Multidimensional NMR Methods for Protein Structure Determination. *IUBMB Life* **2001**, *52* (6), 291–302. https://doi.org/10.1080/152165401317291147.
(77) Gardner, K. H.; Kay, L. E. The Use of 2H, 13C, 15N Multidimensional NMR to Study the Structure and Dynamics of Proteins. *Annu. Rev. Biophys. Biomol. Struct.* **1998**, *27*, 357–406. https://doi.org/10.1146/annurev.biophys.27.1.357.
(78) Hafsa, N. E.; Arndt, D.; Wishart, D. S. CSI 3.0: A Web Server for Identifying Secondary and Super-Secondary Structure in Proteins Using NMR Chemical Shifts. *Nucleic Acids Res.* **2015**, *43* (W1), W370–W377. https://doi.org/10.1093/nar/gkv494.
(79) Güntert, P. Automated NMR Structure Calculation with CYANA. *Methods Mol. Biol. Clifton NJ* **2004**, *278*, 353–378. https://doi.org/10.1385/1-59259-809-9:353.
(80) Norris, M.; Fetler, B.; Marchant, J.; Johnson, B. A. NMRFx Processor: A Cross-Platform NMR Data Processing Program. *J. Biomol. NMR* **2016**, *65* (3–4), 205–216. https://doi.org/10.1007/s10858-016-0049-6.
(81) Herrmann, T.; Güntert, P.; Wüthrich, K. Protein NMR Structure Determination with Automated NOE Assignment Using the New Software CANDID and the Torsion Angle Dynamics Algorithm DYANA. *J. Mol. Biol.* **2002**, *319* (1), 209–227. https://doi.org/10.1016/S0022-2836(02)00241-3.

(82) Shen, Y.; Delaglio, F.; Cornilescu, G.; Bax, A. TALOS+: A Hybrid Method for Predicting Protein Backbone Torsion Angles from NMR Chemical Shifts. *J. Biomol. NMR* **2009**, *44* (4), 213–223. https://doi.org/10.1007/s10858-009-9333-z.
(83) Wüthrich, K. NMR with Proteins and Nucleic Acids. *Europhys. News* **1986**, *17* (1), 11–13. https://doi.org/10.1051/epn/19861701011.
(84) Meng, E. C.; Goddard, T. D.; Pettersen, E. F.; Couch, G. S.; Pearson, Z. J.; Morris, J. H.; Ferrin, T. E. UCSF ChimeraX: Tools for Structure Building and Analysis. *Protein Sci.* **2023**, *32* (11), e4792. https://doi.org/10.1002/pro.4792.
(85) Edgar, R. C. MUSCLE: Multiple Sequence Alignment with High Accuracy and High Throughput. *Nucleic Acids Res.* **2004**, *32* (5), 1792–1797. https://doi.org/10.1093/nar/gkh340.
(86) Kumar, S.; Stecher, G.; Li, M.; Knyaz, C.; Tamura, K. MEGA X: Molecular Evolutionary Genetics Analysis across Computing Platforms. *Mol. Biol. Evol.* **2018**, *35* (6), 1547–1549. https://doi.org/10.1093/molbev/msy096.
(87) Jumper, J.; Evans, R.; Pritzel, A.; Green, T.; Figurnov, M.; Ronneberger, O.; Tunyasuvunakool, K.; Bates, R.; Žídek, A.; Potapenko, A.; Bridgland, A.; Meyer, C.; Kohl, S. A. A.; Ballard, A. J.; Cowie, A.; Romera-Paredes, B.; Nikolov, S.; Jain, R.; Adler, J.; Back, T.; Petersen, S.; Reiman, D.; Clancy, E.; Zielinski, M.; Steinegger, M.; Pacholska, M.; Berghammer, T.; Bodenstein, S.; Silver, D.; Vinyals, O.; Senior, A. W.; Kavukcuoglu, K.; Kohli, P.; Hassabis, D. Highly Accurate Protein Structure Prediction with AlphaFold. *Nature* **2021**, *596* (7873), 583–589. https://doi.org/10.1038/s41586-021-03819-2.
(88) Abramson, J.; Adler, J.; Dunger, J.; Evans, R.; Green, T.; Pritzel, A.; Ronneberger, O.; Willmore, L.; Ballard, A. J.; Bambrick, J.; Bodenstein, S. W.; Evans, D. A.; Hung, C.-C.; O'Neill, M.; Reiman, D.; Tunyasuvunakool, K.; Wu, Z.; Žemgulytė, A.; Arvaniti, E.; Beattie, C.; Bertolli, O.; Bridgland, A.; Cherepanov, A.; Congreve, M.; Cowen-Rivers, A. I.; Cowie, A.; Figurnov, M.; Fuchs, F. B.; Gladman, H.; Jain, R.; Khan, Y. A.; Low, C. M. R.; Perlin, K.; Potapenko, A.; Savy, P.; Singh, S.; Stecula, A.; Thillaisundaram, A.; Tong, C.; Yakneen, S.; Zhong, E. D.; Zielinski, M.; Žídek, A.; Bapst, V.; Kohli, P.; Jaderberg, M.; Hassabis, D.; Jumper, J. M. Accurate Structure Prediction of Biomolecular Interactions with AlphaFold 3. *Nature* **2024**, *630* (8016), 493–500. https://doi.org/10.1038/s41586-024-07487-w.
(89) Franklin, M. J.; Chitnis, C. E.; Gacesa, P.; Sonesson, A.; White, D. C.; Ohman, D. E. Pseudomonas Aeruginosa AlgG Is a Polymer Level Alginate C5-Mannuronan Epimerase. *J. Bacteriol.* **1994**, *176* (7), 1821–1830. https://doi.org/10.1128/jb.176.7.1821-1830.1994.
(90) Hmelo, L. R.; Borlee, B. R.; Almblad, H.; Love, M. E.; Randall, T. E.; Tseng, B. S.; Lin, C.; Irie, Y.; Storek, K. M.; Yang, J. J.; Siehnel, R. J.; Howell, P. L.; Singh, P. K.; Tolker-Nielsen, T.; Parsek, M. R.; Schweizer, H. P.; Harrison, J. J. Precision-Engineering the Pseudomonas Aeruginosa Genome with Two-Step Allelic Exchange. *Nat. Protoc.* **2015**, *10* (11), 1820–1841. https://doi.org/10.1038/nprot.2015.115.
(91) Stookey, L. L. Ferrozine---a New Spectrophotometric Reagent for Iron. *Anal. Chem.* **1970**, *42* (7), 779–781. https://doi.org/10.1021/ac60289a016.
(92) Jeitner, T. M. Optimized Ferrozine-Based Assay for Dissolved Iron. *Anal. Biochem.* **2014**, *454*, 36–37. https://doi.org/10.1016/j.ab.2014.02.026.
(93) Van, V.; Brown, J. B.; O'Shea, C. R.; Rosenbach, H.; Mohamed, I.; Ejimogu, N.-E.; Bui, T. S.; Szalai, V. A.; Chacón, K. N.; Span, I.; Zhang, F.; Smith, A. T. Iron-Sulfur Clusters Are

Involved in Post-Translational Arginylation. *Nat. Commun.* **2023**, *14* (1), 458. https://doi.org/10.1038/s41467-023-36158-z.
(94) George, G. N. *EXAFSPAK*; Stanford Synchrotron Radiation Laboratory, Menlo Park, CA., 1995.
(95) Gurman, S. J.; Binsted, N.; Ross, I. A Rapid, Exact Curved-Wave Theory for EXAFS Calculations. *J. Phys. C Solid State Phys.* **1984**, *17* (1), 143. https://doi.org/10.1088/0022-3719/17/1/019.
(96) Gurman, S. J.; Binsted, N.; Ross, I. A Rapid, Exact, Curved-Wave Theory for EXAFS Calculations. II. The Multiple-Scattering Contributions. *J. Phys. C Solid State Phys.* **1986**, *19* (11), 1845. https://doi.org/10.1088/0022-3719/19/11/021.